Addressing bedload flux variability due to grain shape effects and experimental channel geometry

Thomas Pähtz^{1*}, Yulan Chen^{1*}, Jiafeng Xie^{1,2}, Rémi Monthiller³, Raphaël Maurin⁴, Katharina Tholen⁵, Yen-Cheng Lin⁶, Hao-Che Ho⁶, Peng Hu¹, Zhiguo He¹, Orencio Durán Vinent⁷

Key Points:

- We derive and validate a universal method of bed shear stress determination, applicable to very narrow and/or shallow channels
- We generalize an existing bedload flux model to account for grain shape effects and fluid lift forces
- The model agrees with a very diverse compilation of grain-shape-controlled data sets from first-rate methods

Corresponding author: Thomas Pähtz, 0012136@zju.edu.cn

Corresponding author: Peng Hu, pengphu@zju.edu.cn

Corresponding author: Zhiguo He, hezhiguo@zju.edu.cn

¹Institute of Port, Coastal and Offshore Engineering, Ocean College, Zhejiang University, 316021 Zhoushan, China

²State Key Laboratory of Fluid Power and Mechatronic Systems and Department of Engineering

Mechanics, Zhejiang University, Hangzhou 310027, China
³Aix-Marseille University, CNRS, Centrale Marseille, Institut de Recherche sur les Phénomènes Hors
Équilibre (IRPHÉ), Marseille 13384, France

⁴Institut de Mécanique des Fluides de Toulouse (IMFT), Université de Toulouse, CNRS, F-31400

Toulouse, France 5 Institute for Theoretical Physics, Leipzig University, Postfach 100920, 04009 Leipzig, Germany 6 Department of Civil Engineering, National Taiwan University, Taipei City 106, China 7 Department of Ocean Engineering, Texas A&M University, College Station, Texas 77843-3136, USA

^{*}These authors contributed equally to this work

Abstract

The study-to-study variability of bedload flux measurements in turbulent sediment transport borders an order of magnitude, even for idealized laboratory conditions. This uncertainty stems from physically poorly supported, empirical methods to account for channel geometry effects in the determination of the transport-driving bed shear stress and from study-to-study grain shape variations. Here, we derive a universal method of bed shear stress determination. It consists of a physically-based definition of the bed surface and a channel sidewall correction that does not rely on empirical elements, except for well-established scaling coefficients associated with Kolmogórov's theory of turbulence. Application of this method to bedload transport of spherical grains—to rule out grain shape effects—collapses data from existing laboratory measurements and grain-resolved CFD-DEM simulations for various channel geometries onto a single curve. In contrast, classical sidewall corrections, as well as an alternative bed surface definition, are unable to universally capture these data, especially those from shallow or very narrow channel flows. We then apply our method to an extended grain-shape-controlled data compilation, complemented by literature data for non-spherical grains and from grain-unresolved CFD-DEM simulations. This compilation covers a very diverse range of transport conditions, ranging from very narrow to infinitely wide channels, from shallow to deep channel flows, from mild to steep bed slopes, and from weak to intense transport. We generalize an existing physical bedload flux model to account for grain shape variability and show that it explains almost all the compiled data within a factor of only 1.3.

Plain Language Summary

Sediment transport in the so-called bedload regime occurs when a bed of coarse sedimentary grains becomes mobile by the shearing of a flowing liquid. It shapes the landscapes of Earth and other planetary bodies by promoting the formation and growth of various multiscale geological features. Estimating the rate at which such processes take place requires accurate bedload flux predictions. However, even for idealized laboratory conditions, study-to-study variability of reported bedload flux measurements borders an order of magnitude. This uncertainty stems from physically poorly supported, empirical methods to account for channel geometry effects in the determination of the transportdriving bed shear stress, especially for shallow or very narrow channels, and from studyto-study grain shape variations. Correctly accounting for these effects is a prerequisite for understanding bedload flux variability in more complex natural scenarios. Here, we derive and validate a universal method of bed shear stress determination and apply it to a number of independent grain-shape-controlled data sets from experiments and numerical simulations based on first-rate methods for a very diverse range of transport conditions and channel geometries. An existing physical bedload flux model, generalized to account for grain shape variability, predicts almost all these data within a factor of 1.3.

1 Introduction

Bedload transport is a special kind of sediment transport in which typically coarse sedimentary grains roll, slide, and hop along the surface in response to the shearing of a loose granular bed by a flow of liquid. It plays a vital role in shaping the environments of Earth and other planetary bodies (Poggiali et al., 2016) by promoting the formation and growth of geological features of various scales, including ripples and dunes (Charru et al., 2013; Durán Vinent et al., 2019), deltas and fans (Baker et al., 2015), and laminations and cross-bedding (Schieber, 2016; Shchepetkina et al., 2019). A key problem hampering our understanding of bedload-induced landscape evolution is the notoriously large noise commonly associated with measurements of the bedload flux, often exceeding an order of magnitude (Recking, 2010; Ancey & Recking, 2023). It partially originates from huge non-Gaussian flux fluctuations over large time scales, which even oc-

cur under steady flow conditions in the laboratory due to continuous topographic change (Dhont & Ancey, 2018). However, also when restricted to steady flows over flat beds at short timescales, reported bedload fluxes can still substantially differ between laboratory studies for largely self-similar conditions, for both weak and intense transport-driving flows (Ancey & Recking, 2023), and it has been unclear whether such differences arise due to physical or experimental reasons. On the one hand, physical reasons may come into play because dissimilarities in grain size and shape distributions are not accounted for by commonly used similarity parameters. On the other hand, study-to-study variability of the geometry of laboratory facilities is a potential culprit on the experimental side, especially in view of the associated large random and systematic uncertainties in the experimental determination of the transport-driving bed shear stress τ_b (Yager et al., 2018). Focusing here on rectangular open channels, since they are geometrically similar to natural streams, the ratio b/h between the channel width b and flow depth h is a crucial parameter in this regard. Ideally, one would want b/h to be as large as possible to most closely resemble bedload transport in nature. However, in experimental reality, b/h is often of order unity, substantially weakening the shearing of the bed due to frictional losses at the sidewalls, causing the flow to be nonuniform in the cross-channel direction (Guo, 2015). Another important parameter is the ratio between h and the grain diameter d. For shallow channel flows where h/d is close to unity, the method by which the bed surface elevation, and thus the flow depth h above it, is identified can have a large effect on the value of τ_h .

To exemplary illustrate that channel geometry effects often are not appropriately accounted for, we choose two laboratory studies measuring bedload flux over a flat bed: Ni and Capart (2018), who conducted their experiments in a wide but shallow channel $(h/d \sim 2 \dots 6)$, and Deal et al. (2023), who used a very narrow but deep channel $(b/h \approx 0.1)$. Since the grains in both studies were spherical and relatively uniformly sized, one expects the same quantitative behavior of the nondimensionalized bedload flux Q_* as a function of the nondimensionalized bed shear stress or Shields number Θ (Ancey, 2020). However, when using these studies' reported values for Θ and Q_* , based on their own definitions and methods to determine τ_b , both data sets disagree from each other by a staggering factor of about 6 for $\Theta \approx 0.2$ (figure 1). This indicates that at least one of them was inappropriately correcting for channel geometry effects, showcasing the need for a universal channel geometry correction method.

This study addresses two of the mentioned potential reasons for the study-to-study variability of laboratory bedload flux measurements: grain shape and channel geometry effects. We compile existing and new data of turbulent bedload transport of shapecontrolled and (relatively) uniformly sized grains, obtained from experiments and grainresolved (i.e., directly resolving fluid-particle interactions) and grain-unresolved numerical simulations based on various Computational Fluid Dynamics-Discrete Element Method (CFD-DEM) techniques, across channel flow widths and heights, grain shapes, bed slopes, and flow strengths. In §2, we reconcile channel geometry effects in these data through a universal sidewall correction, which we rigorously derive from an extension of Kolmogórov's theory of turbulence (Gioia & Bombardelli, 2002; Gioia & Pinaki Chakraborty, 2006), and a granular-physics-based definition to precisely determine the bed surface elevation (Pähtz & Durán, 2018b). This channel geometry correction method is validated, among others, through a collapse of experimental and grain-resolved numerical bedload flux data for spherical grains on a unique behavior, whereas classical methods (Einstein, 1942; Johnson, 1942; Guo, 2015, 2017) yield very large scatter. Furthermore, in §3, we generalize an existing physical bedload flux model (Pähtz & Durán, 2020) to account for grain shape variability. It agrees with the entire channel-geometry-corrected data compilation within a factor of 1.3. The results are then discussed in §4 and conclusions are drawn in §5.

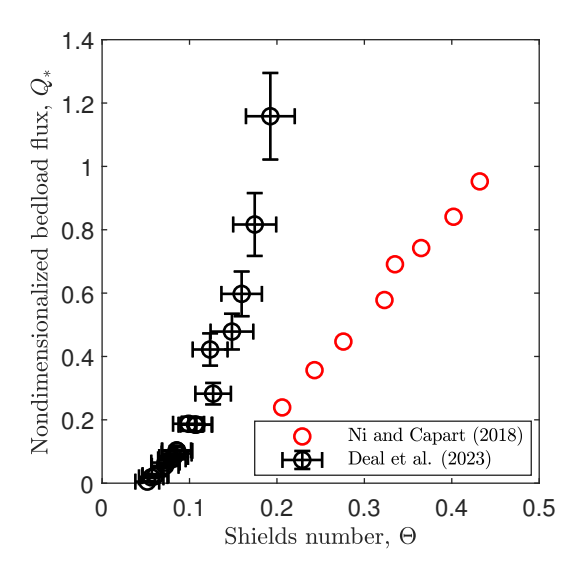


Figure 1. Bedload flux measurements for spherical grains by Ni and Capart (2018) and Deal et al. (2023). The Shields number Θ and nondimensionalized bedload flux Q_* were defined and determined as described in these studies. For $\Theta \approx 0.2$, the values of Q_* disagree from each other by a factor of about 6.

2 Universal channel geometry correction method

In this section, we derive and validate a universal channel geometry correction method to determine the transport-driving bed shear stress τ_b . We begin with the definition of τ_b (§2.1) and derive from it, partially using known results, an expression that contains the flow depth h and the effective mixture sidewall shear stress τ_w as unknowns. We then propose to determine h from an existing granular-physics-based definition of the bed surface elevation (§2.2) and derive an expression for τ_w/τ_b from an extension of Kolmogórov's theory of turbulence (§2.3). In §2.4, the resulting channel geometry correction method is tested against a data compilation of turbulent bedload transport of spherical grains and other data.

2.1 Definition of bed shear stress

For turbulent bedload transport in open channels, there is a limited region in the clear-water flow above the bedload layer where the streamwise (x) fluid velocity profile $u_x(z)$ approximately obeys the logarithmic law of the wall (Kidanemariam, 2016; Jain et al., 2021; Deal et al., 2023):

$$u_x \simeq \frac{u_\tau}{\kappa} \ln \frac{z + z_o}{z_o},\tag{1}$$

where $\kappa=0.41$ is the von Kármán constant, z the bed-normal coordinate, with z=0 the bed surface elevation, z_o the hydrodynamic roughness, and u_τ the friction velocity. The latter defines the bed shear stress $\tau_b \equiv \rho_f u_\tau^2$, where ρ_f is the fluid density. In what follows, we seek to express τ_b in terms of known fluid and channel parameters.

Kidanemariam (2016) and Jain et al. (2021) conducted DNS-DEM simulations of bedload transport driven by negative streamwise fluid pressure gradients χ at zero bed slope angle α for infinitely wide and relatively deep channel flows. Both studies found that τ_b defined via equation (1) is equivalent to the effective mixture shear stress evaluated at the bed surface, $\tau_{zx}(0)$. Below, we generalize this result to open channels with sidewalls and arbitrary α .

For a statistically steady ($\partial_t = 0$) and streamwise uniform ($\partial_x = 0$) open channel flow, the mixture momentum balance resulting from averaging over time t and the streamwise direction x reads (Pähtz et al., 2025)

$$\partial_y \tilde{\rho} \tilde{u}_y \tilde{u}_x + \partial_z \tilde{\rho} \tilde{u}_z \tilde{u}_x = \partial_y \tilde{\tau}_{yx} + \partial_z \tilde{\tau}_{zx} + \chi + \tilde{\rho} g \sin \alpha, \tag{2}$$

where g is the gravitational acceleration, $\tilde{\rho}$ the mixture density, $\tilde{\boldsymbol{u}}$ the mixture velocity, and $\tilde{\boldsymbol{\tau}}$ the mixture shear stress tensor, which is composed of the averaged viscous fluid shear stress, the solid phase contact stress, a stress resulting from fluid-particle interactions, and the mixture Reynolds stress. Integrating equation (2) over height and the cross-channel coordinate y, written using the notations $\langle \cdot \rangle_z \equiv \frac{1}{h} \int_0^h \cdot \mathrm{d}z$ and $\langle \cdot \rangle_y \equiv \frac{1}{b} \int_{-b/2}^{b/2} \cdot \mathrm{d}y$, then yields

$$-b\left[\langle \tilde{\tau}_{zx} - \tilde{\rho}\tilde{u}_z\tilde{u}_x \rangle_y\right]_{z=0}^{z=h} = h\left[\langle \tilde{\tau}_{yx} - \tilde{\rho}\tilde{u}_y\tilde{u}_x \rangle_z\right]_{y=-b/2}^{y=b/2} + bh\chi + bh\langle\langle \tilde{\rho} \rangle_y \rangle_z g \sin \alpha. \tag{3}$$

When assuming impermeable boundary conditions at the bed $(\tilde{\rho}\tilde{u}_z)_y(0) = 0$ and free surface $(\tilde{\rho}\tilde{u}_z)_y(h) = 0$) on average, then statistical steadiness and mass conservation would imply impermeable boundary conditions also at the sidewalls $(\langle \tilde{\rho}\tilde{u}_{y}\rangle_{z}(\pm b/2) =$ 0) on average, and vice versa. Although these boundaries are not necessarily perfectly impermeable, since low vertical transport may occur through the bed surface, we assume impermeability for simplicity, in which case the terms $-\langle \tilde{\rho}\tilde{u}_z\tilde{u}_x\rangle_y(0,h)$ and $-\langle \tilde{\rho}\tilde{u}_y\tilde{u}_x\rangle_z(\pm b/2)$ are Reynolds-like fluctuation stresses. We therefore identify $\tau_{zx} \equiv \langle \tilde{\tau}_{zx} - \tilde{\rho} \tilde{u}_z \tilde{u}_x \rangle_y$, when evaluated at z = 0 or z = h, as the effective mixture bed and free-surface shear stresses, respectively, and $\tau_w \equiv \mp (\langle \tilde{\tau}_{yx} - \tilde{\rho} \tilde{u}_y \tilde{u}_x \rangle_z)(\pm b/2)$ as the effective mixture sidewall shear stress. Furthermore, we use the free-surface boundary condition $\tau_{zx}(h)=0$ and the relation $\langle \tilde{\rho} \rangle_y = (1 - \phi) \rho_f + \phi \rho_p$ (Pähtz et al., 2025), where ρ_p is the particle density and $\phi(z)$ the cross-channel-averaged particle volume fraction, and define the sediment transport load $M \equiv \rho_p h \langle \phi \rangle_z$ (the average mass of transported grains—i.e., grains elevated above the bed surface—per unit area of the bed surface) and the vertical submerged gravitational acceleration $\tilde{g}_z \equiv (1-\rho_f/\rho_p)g\cos\alpha$. Inserting these relations and definitions, and dividing by b, equation (3) becomes

$$\tau_{zx}(0) = h(\chi + \rho_f g \sin \alpha) - (2h/b)\tau_w + M\tilde{g}_z \tan \alpha. \tag{4}$$

This expression is a generalization of the mixture balance by Bagnold (1956) to the case of a channel with sidewalls (h/b > 0) and of the clear-water balance by Guo (2015) to the case of a mixture (M > 0); both studies also assumed $\chi = 0$. Since we later propose a Bagnoldian-type bedload model, we assume analogous to Bagnold (1956) that the bed shear stress defined via equation (1) is given by

$$\tau_b = \tau_{zx}(0) - M\tilde{g}_z \tan \alpha. \tag{5}$$

This assumption is the generalization of the mentioned finding $\tau_b = \tau_{zx}(0)$ for $\alpha = 0$ (Kidanemariam, 2016; Jain et al., 2021). Note that the alternative assumption that $\tau_b = \tau_{zx}(0)$ for all α would lead to inconsistencies later on. Combining equations (4) and (5) yields

$$\tau_b = h(\chi + \rho_f g \sin \alpha) - (2h/b)\tau_w. \tag{6}$$

Here τ_b depends on two unknowns: the bed surface elevation z=0 required to determine h and the effective mixture sidewall shear stress τ_w . They are addressed below.

2.2 Definition of bed surface elevation

Typically, distinct definitions of the bed surface elevation z=0 differ from one another by a fraction of the grain size d. Therefore, for deep channel flows $(h \gg d)$, the identification of the bed surface elevation is quantitatively not so important for the determination of τ_b and standard $ad\ hoc$ definitions do the job reasonably well. However,

for shallow channel flows, the situation is fundamentally different and a definition that accounts for the grain-scale physical processes is required.

We propose that the definition by Pähtz and Durán (2018b) should be used to determine h. It is based on the local particle pressure $-\sigma_{zz}^p$ and particle shear rate $\dot{\gamma}=\mathrm{d}_z v_x$, with $\boldsymbol{v}(z)$ the average particle velocity. Their product halved, $-\frac{1}{2}\sigma_{zz}^p\dot{\gamma}$, describes the rate at which the flow converts mean energy density into the pseudo-kinetic fluctuation energy density $-\frac{1}{2}\rho_p\phi v_z v_x$ (half the particle Reynolds stress). This rate is expected to peak as a result of particle-bed collisions, leading to the following indirect definition of the bed surface elevation:

$$\max(\dot{\gamma}\Sigma\phi) = (\dot{\gamma}\Sigma\phi)(0),\tag{7}$$

with $\Sigma \phi(z) \equiv \int_z^h \phi(z') dz'$, based on the approximation $-\sigma_{zz}^p \approx \rho_p \Sigma \phi$.

Apart from being used to determine h, the bed surface elevation defined by equation (7) has two important physical properties (Pähtz & Durán, 2018b): First, the ratio $\mu_b \equiv -\tau_{zx}^p(0)/\sigma_{zz}^p(0)$ between the bed surface particle shear stress $\tau_{zx}^p(0)$ and particle pressure $-\sigma_{zz}^p(0)$ is approximately constant. Second, except for intense transport conditions, the bed surface fluid shear stress $\tau_{zx}^f(0)$ reduces to approximately the threshold shear stress τ_t . These two properties are sometimes referred to as Bagnold's hypotheses and integral parts of Bagnoldian-type bedload models (Pähtz & Durán, 2018b, and references therein). In particular, given sufficiently highly resolved data, they can be used as an independent consistency check of the definition in equation (7).

2.3 Sidewall correction

Equation (6) is the same as that for clear-water flow (Guo, 2015), except for generalized meanings of τ_b and τ_w . In particular, the bed shear stress τ_b , even though it is based on the mixture flow above the bed surface, controls, like its clear-water counterpart, the slope of the logarithmic velocity profile in equation (1) (Kidanemariam, 2016; Jain et al., 2021; Deal et al., 2023). Like previous studies on the sidewall correction for open channel flows with sediment transport (Einstein, 1942; Johnson, 1942; Vanoni & Brooks, 1957; Guo, 2015), we therefore model τ_b and τ_w as if the the flow above the bed surface was clear-water flow.

We start with rearranging equation (6) into the form

$$\tau_b = \frac{h(\chi + \rho_f g \sin \alpha)}{1 + \frac{2h}{b} f_w / f_b},\tag{8}$$

where $f_w \equiv \tau_w/(\rho_f U^2)$ and $f_b \equiv \tau_b/(\rho_f U^2)$ are the friction factors associated with the sidewalls and bed surface, respectively, with U the bulk fluid flow velocity. The rougher these surfaces are, the larger is the rate at which the bulk flow energy density $\rho_f U^2/2$ is frictionally dissipated, and the larger is the shear stress applied at them. The difficulty is now to relate the friction factor ratio f_w/f_b to the sidewall and bed surface roughnesses and the bulk flow properties.

A classical approach employed in numerous studies is to assume $f_w = f_b$, in which case $\tau_b = \tau_R \equiv R(\langle \chi \rangle_z + \rho_f g \sin \alpha)$, with $R \equiv hb/(b+2h)$ the hydraulic radius of the open channel (Guo, 2015). This prediction is consistent with measurements of flow velocity profiles in particle-free open channels consisting of only smooth walls (sidewalls and bottom wall) for a large range of width-to-depth ratios (b/h = 1.04-9.5) (Yang et al., 2005). However, in bedload transport, where the bed surface is typically rougher than the smooth sidewalls ($f_b > f_w$), τ_R merely constitutes a lower bound of τ_b .

Another classical approach is the one by Einstein-Johnson (Einstein, 1942; Johnson, 1942; Vanoni & Brooks, 1957; Guo, 2017) (Appendix A), in which f_w is determined from the empirical Karman-Prandtl law as the friction factor of a fully smooth channel

and then f_b linked to f_w via an ad hoc separation of the open channel into three parallel, non-interacting sidewall-free channels. However, this separation's only physical justification is its mathematically constructed consistency at the extreme limit $f_b = f_w$, where it rightfully predicts $\tau_b = \tau_R$.

Our approach presented below does not rely on Einstein's ad hoc channel separation but instead employs, for the Reynolds shear stress τ_s at a given surface (the sidewalls or the bed surface), a relation based on Kolmogórov's theory of turbulence (Gioia & Bombardelli, 2002; Gioia & Pinaki Chakraborty, 2006):

$$\tau_s = -\rho_f \langle u'_{\parallel} u'_{\perp} \rangle = \kappa_\tau \rho_f U u_s, \tag{9}$$

where $\langle \cdot \rangle$ denotes an averaging procedure and κ_{τ} is a flow-geometry-dependent empirical coefficient. Equation (9) states that the surface-parallel velocity fluctuations u'_{\parallel} are dominated by the largest turbulent eddies in the system, whose characteristic velocity is U, whereas the surface-normal velocity fluctuations u'_{\perp} are primarily controlled by the largest normal velocities u_s that turbulent eddies can generate near the surface. This relation, which was previously used to physically derive Manning's (Gioia & Bombardelli, 2002) and Nikuradse's (Gioia & Pinaki Chakraborty, 2006) empirical formulas, leads to $f_w/f_b = u_w/u_b$, where u_b and u_w are the values of u_s for the rough bed surface and smooth sidewalls, respectively. The sizes of the eddies governing u_b and u_w are controlled by the roughness size r of the rough bed and the thickness $5(\kappa_\epsilon \kappa_u^3/2)^{-1/4} R \Re^{-3/4}$ of the viscous sublayer adjacent to the smooth sidewalls (Gioia & Pinaki Chakraborty, 2006), respectively, where $\Re \equiv UR/\nu$ is the bulk flow Reynolds number, with ν the kinematic fluid viscosity. Furthermore, $\kappa_{\epsilon} = 5/4$ is a constant that follows from Kolmogórov's fourfifths law and $\kappa_u \equiv u_R/U$ a parameter that relates the characteristic velocity u_R of the largest eddies to U. It is found to be largely insensitive to flow geometry, with $\kappa_u = 0.036 \pm$ 0.005 measured in pipe flow (Antonia & Pearson, 2000) and $\kappa_u = 0.033$ in the atmospheric boundary layer (Tennekes & Lumley, 1972). With these parameters, $f_w/f_b =$ u_w/u_b can be calculated by equation (2) of Gioia and Pinaki Chakraborty (2006) as

$$\frac{f_w}{f_b} = \frac{\left[5(\kappa_\epsilon \kappa_u^3/2)^{-1/4} R \Re^{-3/4}\right]^{1/3} \sqrt{(\beta/5)^{2/3} \Gamma_{-2/3} (\beta/5)}}{r^{1/3}} = c_{wb} \Re^{-1/4} (r/R)^{-1/3}, \quad (10)$$

where $\Gamma_{-2/3}$ is the gamma function of order -2/3, $\beta = [3\Gamma(4/3)]^{3/4}$ the characteristic constant of the exponential decay of the velocity spectrum of turbulent flow, with Γ the gamma function, and $c_{wb} \simeq 2.23$ is the scaling coefficient resulting from evaluating the expression in the middle of equation (10). Since it depends only on κ_{ϵ} , κ_{u} , and β , but not on the parameter κ_{τ} defined through equation (9), c_{wb} is an approximately channel-geometry-independent parameter.

In order to use equation (10), one needs to know the bulk fluid flow velocity U and bed roughness size r. We calculate the former from the fluid discharge Q_f as (Rebai et al., 2022)

$$U = \frac{Q_f}{b\left(h - \int_0^h \phi dz\right)}.$$
 (11)

Note that, except for intense bedload transport, the term $\int_0^h \phi dz$ has only a marginal effect on τ_b . Hence, for the data sets by Deal et al. (2023), which will constitute a part of our data compilation and for which concentration profile data is not available, we calculate U as $U \simeq Q_f/(bh)$.

In clear-water open channels consisting of rough beds and smooth sidewalls, the bed roughness size r is sometimes directly accessible (Auel et al., 2014) or can be approximated as the volume-equivalent sphere diameter $d_o \equiv \sqrt[3]{6V_p/\pi}$ of the grains composing the manually prepared fixed bed (Song & Chiew, 2001), where V_p is the grain volume. However, in the context of bedload transport over mobile beds, a more sophisti-

cated estimate is required. Since grains transported at elevations close to the bed surface tend to align their largest projected area parallel to the bed due to torque (Jain et al., 2020; Zhang et al., 2025), we choose the shortest grain axis c_g as the parameter setting r. It complements the large (a_g) and intermediate (b_g) grain axes, defined through approximating grains as ellipsoids. Hence, assuming that the bed is protruding into the flow by about half the grain size for water-worked beds, as opposed to the typical full exposure in manually prepared fixed beds, we obtain $r = c_g/2$ for sediment transport applications.

2.4 Validation of channel geometry correction method

2.4.1 Data compilation for bedload transport of spherical grains

In order to isolate channel geometry effects on bedload flux, we compile existing experimental data sets for spherical grains, assuming that grain shape effects are negligible for them. However, surprisingly, even though turbulent bedload transport has been studied for more than a century (Ancey, 2020), flux measurements for spherical grains with a nearly uniform size distribution seem to be exceedingly scarce. After an extensive literature search, we have managed to find only a handful of data sets (Ni & Capart, 2018; Frey et al., 2006; Frey, 2014; Armanini & Cavedon, 2019; Carrillo et al., 2022; Deal et al., 2023). Four of these were subsequently disregarded because of either partially crystallized beds and very large scatter (Frey et al., 2006; Frey, 2014), or the presence of substantial suspended load in addition to bedload (Armanini & Cavedon, 2019), or self-inconsistent data (Carrillo et al., 2022) (almost no bedload flux change with important variation of flow strength: increasing bed slope at constant flow depth). The only two remaining experimental data sets for spherical grains are those by Deal et al. (2023) and Ni and Capart (2018) discussed in the introduction. We therefore supplement the data compilation with additional data sets from numerical simulations that couple the DEM for the particle phase with a CFD method for the fluid phase that resolves the sub-grain scale: two data sets based on Direct Numerical Simulations (DNS) (Jain et al., 2021; Kidanemariam & Uhlmann, 2017) for infinitely wide channels $(b/h = \infty, i.e., periodic bound$ aries) and two data sets based on grain-resolved Large Eddy Simulation (LES) (Zhang et al., 2022): one for $b/h = \infty$ and one for a narrow-deep-channel configuration $(b/h \approx$ 0.1). Only such high-end methods, because they do not coarse-grain the particle phase and do not rely on empiricism for fluid-particle interactions, can be considered as similarly reliable as controlled experiments. The above spherical-grain data sets are denoted as D23EXPs, NC18EXP, Z22LESn, Z22LESw, J21DNS, and KU17DNS, and summarized in Table 1 together with other data sets used later.

For the data sets discussed in the previous paragraph, we determine the bed surface elevation using the method described in §2.2, provided the required data are available from the studies. This is the case for the data set NC18EXP (figure 2), but not for D23EXPs, Z22LESn, Z22LESn, J21DNS, and KU17DNS. For the latter, we use the values reported in the respective studies. This approximation is justified for D23EXPs, Z22LESn, J21DNS, and KU17DNS, since $h^* = h/d \gg 1$ (Table 1). In the case of Z22LESw, the authors of the respective study (Zhang et al., 2022) stated that they employed the method by Pähtz and Durán (2018a) to calculate the bed surface elevation, which is the same as our method described in §2.2. For more details and the calculation of the bed shear stress uncertainty, see Appendix B.

2.4.2 Test of channel geometry correction methods against data compilation

In this subsection, we test our and existing channel geometry correction methods against the spherical-grain data compilation discussed above. Once the bed shear stress τ_b is determined using a given channel geometry correction method, we are able to fully

simulations, and grain-unresolved CFD-DEM simulations, respectively. Those data of the data sets BLRANS1 and BLRANS2 with s=2.65 and $\alpha=0$ are from Pähtz and Durán (2020). The data set Z25LES does not include data from simulations based on the "artificial-shrinkage method" by Zhang et al. (2025), since this method does probably not correspond to physically realistic scenarios (Chen et al., 2025). Note that the here listed values of C_D , G_a , and h^* for the data of Zhang et al. (2022, 2025); Deal et al. (2023) (Z22LESx, Z25LES, D23EXPx, where 'x' stands for an arbitrary character) can differ from those reported in these references Table 1. Summary of bedload flux data shown in this study. The top, middle, and bottom entries correspond to experiments, grain-resolved CFD-DEM due to a different definition of d.

D'un conjectorated on	117:24th 2000th	5:5%	Chorn	50	040		Decition of an one of the	11:000	
numerical study	ratio, b/h	shape	$\begin{vmatrix} S_f \end{vmatrix}$	S_f C_D μ_s	μ_s	8	ry ur our mannie Ga		h^*
D23EXPs (Deal et al., 2023)	0.09-0.16	spheres		0.43	0.46	2.57	1334-1339	0.03-0.13	13-24
D23EXPe (Deal et al., 2023)	0.10 - 0.14	ellipsoids	0.83	0.60	0.60	2.42	1312 - 1314	0.03 - 0.09	15 - 22
D23EXPc (Deal et al., 2023)	0.10 - 0.13	chips	0.51	0.39	0.65	2.36	267-768	0.04 - 0.08	22 - 29
D23EXPg (Deal et al., 2023)	0.10 - 0.15	gravel	0.68	0.54	0.78	2.48	733-735	0.04 - 0.11	20 - 32
D23EXPp (Deal et al., 2023)	0.09 - 0.12	prisms	0.88	0.79	0.86	2.40	725	0.03 - 0.06	26 - 35
NC18EXP (Ni & Capart, 2018)	5.2 - 7.5	$_{ m spheres}$	П	0.49	0.45	1.39	866	0.02 - 0.03	2.3 - 3.3
R22EXPc (Rebai et al., 2022)	5.5 - 5.6	cylinders	0.84	0.32	0.60	1.42	738	0.05 - 0.06	8.4 - 14
R22EXPI (Rebai et al., 2022)	5.0 - 5.8	lenses	0.55	0.45	0.62	1.37	196	0.03 - 0.05	16 - 18
Z22LESn (Zhang et al., 2022)	0.15-0.16	spheres	П	0.48	0.45	2.55	1354-1357	0.04-0.10	13-14
Z25LES (Zhang et al., 2025)	0.09 - 0.10	gravel	0.67	0.71	0.75	2.47	718 - 719	0.03 - 0.10	32 - 33
Z22LESw (Zhang et al., 2022)	8	$_{ m spheres}$	П	0.48	0.45	2.55	1378	0.01 - 0.03	4.6 - 22
J21DNS (Jain et al., 2021)	8	$_{ m spheres}$	П	N/A	N/A	2.55	44.7	$(0 < \chi) 0$	$\approx \frac{18}{8}$
KU17DNS (Kidanemariam & Uhlmann, 2017)	8	spheres		N/A	N/A	2.5	28.37	$(0 < \chi) 0$	≈ 13
M18RANS (Maurin et al., 2018)	8	spheres	П	0.42	0.40	1.75-4	1259-2521	0.01 - 0.19	2.0-62
M19RANSs (Monthiller, 2019)	8	$_{ m spheres}$	П	0.42	0.49	2.5	1782	0.05	4.1 - 18
M19RANSt1 (Monthiller, 2019)	8	$\operatorname{triplets}$	0.85	0.42	0.55	2.5	1782	0.05	6.1 - 26
M19RANSt2 (Monthiller, 2019)	8	$\operatorname{triplets}$	0.75	0.42	0.63	2.5	1782	0.05	8.0 - 33
M19RANSt3 (Monthiller, 2019)	8	$\operatorname{triplets}$	0.71	0.42	0.68	2.5	1782	0.05	9.9 - 40
M19RANSt4 (Monthiller, 2019)	8	$\operatorname{triplets}$	0.62	0.42	0.72	2.5	1782	0.05	12 - 47
M19RANSt5 (Monthiller, 2019)	8	$\operatorname{triplets}$	0.58	0.42	0.69	2.5	1782	0.05	14 - 55
LES	8	$_{ m spheres}$	П	0.54	0.49	2.56	1341	$(0 < \chi) 0$	18 - 22
LESCD	8	$_{ m spheres}$	_	1.78	0.49	2.56	1341	$(0 < \chi) 0$	20 - 23
BLRANS1	8	$_{ m spheres}$	_	2.24	0.38	[1.1, 2.65]	20	0 - 0.16	8
BLRANS2	8	$_{ m spheres}$	П	1.46	0.38	[1.1, 2.65]	100	0	8
BLRANSCD	8	$_{ m spheres}$		15.9	0.38	2.65	20	0	8

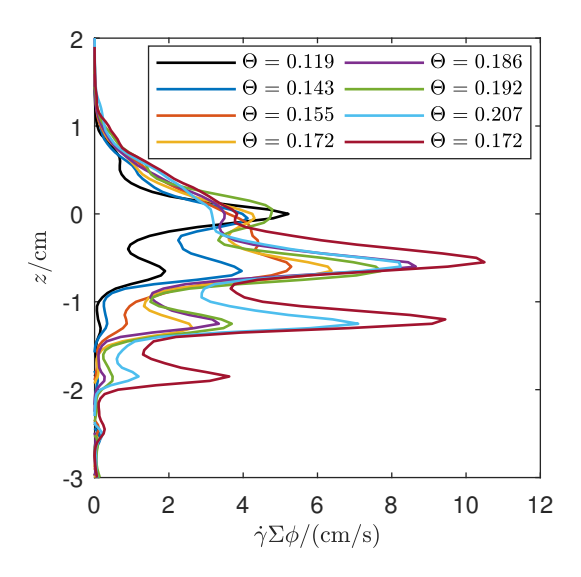


Figure 2. Determination of bed surface elevation for experimental data set NC18EXP (Ni & Capart, 2018). The vertical profiles of $\dot{\gamma}\Sigma\phi$ exhibit several local maximums due to layering. We choose the top-most local maximum as the bed surface elevation because the vertical profile of the fluid shear stress $\tau_{zx}^f(z)$ exhibits a focal point there, with $\tau_{zx}^f(0) \approx \tau_t$ (§2.4.3), consistent with the theoretical expectation (Pähtz & Durán, 2018b).

characterize the hydrodynamic bedload transport conditions by dimensionless similarity parameters. We choose the particle-fluid density ratio $s \equiv \rho_p/\rho_f$, Galileo number $Ga \equiv d\sqrt{s\tilde{g}_zd}/\nu$, Shields number $\Theta \equiv \tau_b/(\rho_p\tilde{g}_zd)$, dimensionless flow depth $h^* \equiv h/d$, and bed slope angle α (Table 1). All spherical-grain data sets (and also those for nonspherical grains considered later) are well within the range of what is typically categorized as bedload transport ($s \lesssim 10$, Pähtz & Durán, 2020), and most of them also satisfy $s^{1/2}Ga \gtrsim 70$, here termed "rough" conditions. In rough turbulent bedload, particle inertia dominate viscous fluid-particle interactions, and the nondimensionalized bedload flux $Q_* \equiv Q/(\rho_p d\sqrt{s\tilde{g}_z d})$ is therefore expected to become essentially independent of s and Ga for sufficiently small α (Pähtz & Durán, 2020; Ancey, 2020). We use this expectation as a tool to evaluate the different sidewall corrections outlined above (figure 3). It can be seen that the data for rough turbulent bedload transport of spherical grains, indeed, collapse, within measurement uncertainty, on a universal $Q_*(\Theta)$ -behavior for our method (figure 3D), but do not collapse at all when employing a classical method or left uncorrected (figures 3A-3C), or when using our sidewall correction but a different bed surface definition (NC18EXP* in figure 3D). The only rough-turbulent-bedload data set that slightly deviates from the collapse in figure 3D is the data set Z22LESn in Table 1 (the data labeled as Z22LESn* in figure 3). This is understandable given that the grid resolution of the grain-resolved LES simulations behind these data was limited to 15 times the Kolmogórov length scale (Zhang et al., 2022), meaning that Kolmogórov's theory of turbulence cannot be applied to them in a strict sense. However, an empirical reduction of this theory's predicted scaling factor $c_{bw} = 2.23$ in equation (10) by 20% to $0.8 \times 2.23 \simeq 1.78$ leads to a data collapse (the data labeled as Z22LESn in figure 3). Henceforth, we apply this reduction to the narrow-channel data sets based on these simulations (Z22LESn and Z25LES) without further notice.

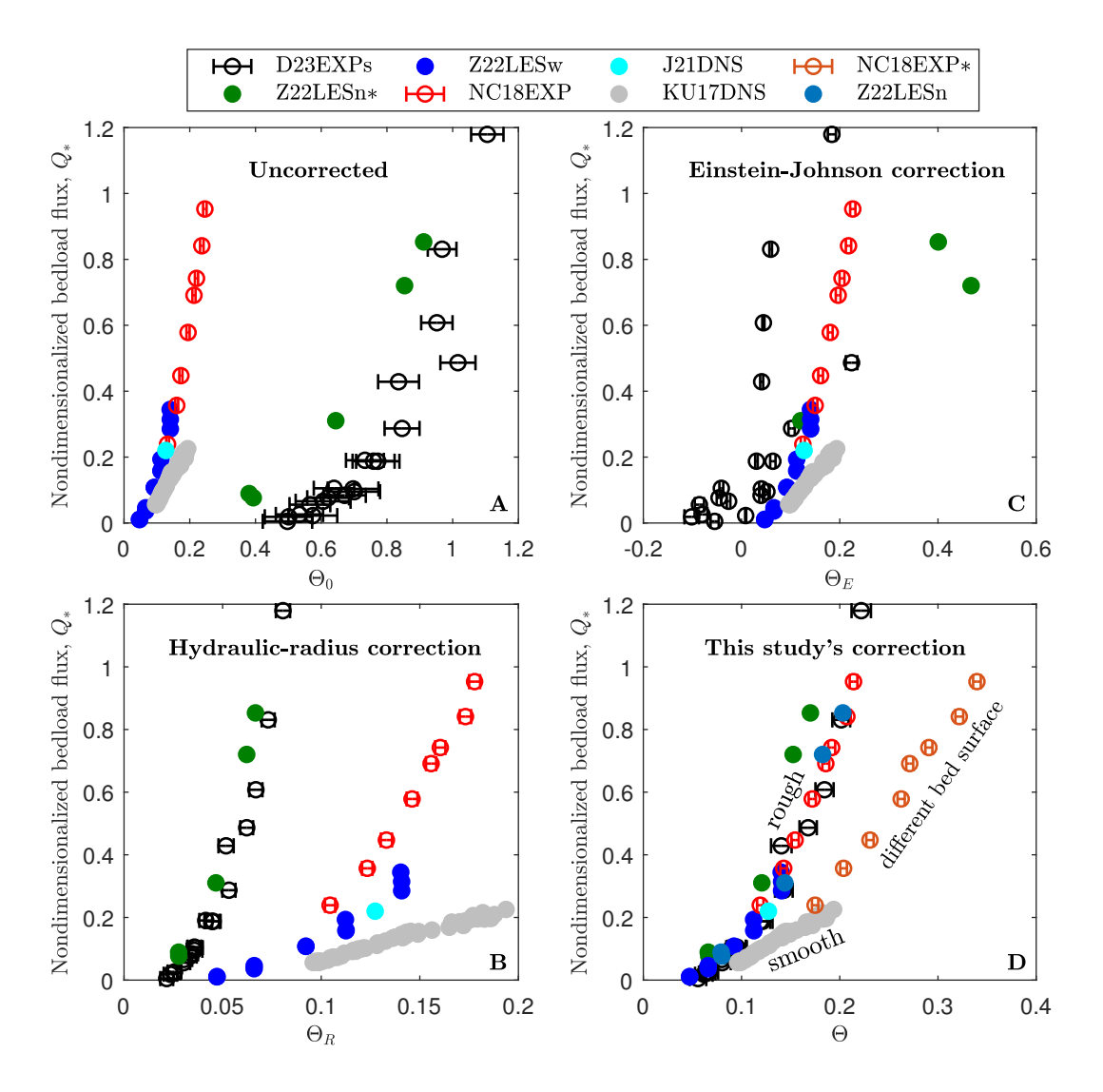


Figure 3. Channel geometry corrections. Nondimensionalized bedload flux Q_* versus Shields numbers for spherical grains: (A) uncorrected for sidewall effects (Θ_0), (B) hydraulic-radius correction (Guo, 2015) (Θ_R), (C) Einstein-Johnson correction (Einstein, 1942; Johnson, 1942; Vanoni & Brooks, 1957; Guo, 2017) (Θ_E), (D) our universal correction (Θ). Symbols correspond to data from experiments and grain-resolved simulations (Table 1). An error bar indicates the standard error and/or uncertainty range. In the absence of error bars, uncertainties are smaller than the symbol size. Except for KU17DNS ($s^{1/2}Ga \simeq 44.86$, smooth), all data are in the rough regime ($s^{1/2}Ga > 70$). The values of h used to determine τ_b in Z22LESw and NC18EXP are based on a granular-physics-based bed surface definition (Pähtz & Durán, 2018b), equation (7), and in NC18EXP* on the original definition reported by Ni and Capart (2018). For all other data sets, reported values of h are used as it has a negligible effect on the Shields numbers. Z22LESn* refers to unmodified data, whereas for Z22LESn in (D), the sidewall correction, and thus Θ , has been modified to account for the fact that the grid resolution of the grain-resolved LES simulations behind these data was limited to 15 times the Kolmogórov length scale (see text).

2.4.3 Further independent tests of our channel geometry correction method

Figures 4A and 4B present further independent support for our sidewall correction. First, our correction predicts almost the same Shields numbers as those Deal et al. (2023) empirically determined as $\tau_b = 2.41\tau_R$ via fitting equation (1) to their flow velocity data, both for spherical and non-spherical grains (figure 4A).

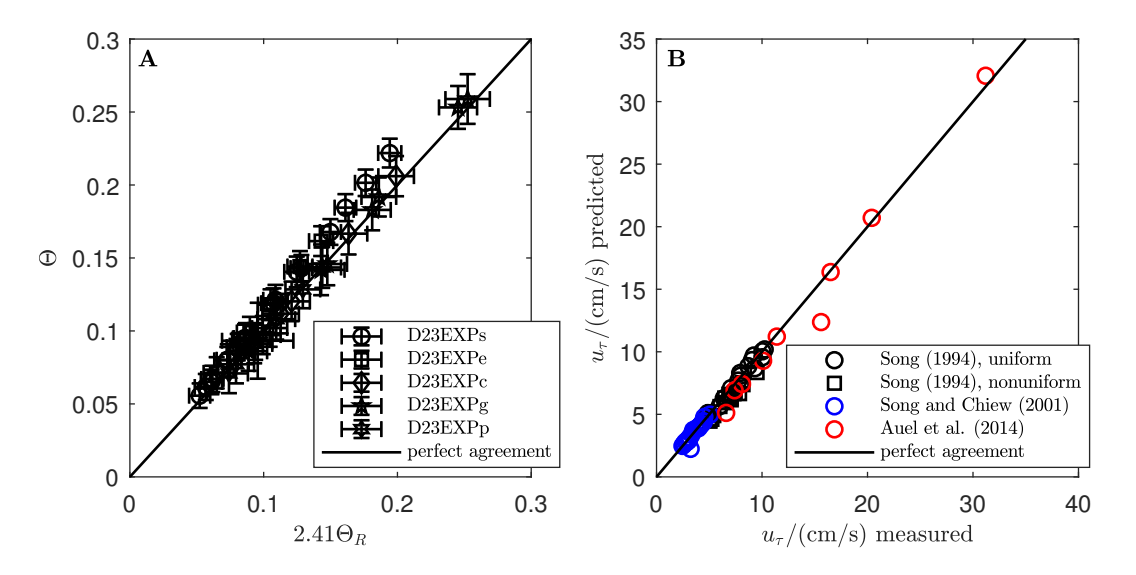


Figure 4. Channel geometry corrections. (A) Θ versus $2.41\Theta_R$ (using $d=c_g$ for non-spherical-grain data, as explained in §3.1.1), based on $\tau_b=2.41\tau_R$, the empirical correction in Deal et al. (2023). (B) Log-profile shear velocity $u_\tau\simeq\sqrt{\tau_b/\rho_f}$ predicted by our sidewall correction versus measured one for experimental data from particle-free flows in open channels consisting of rough beds and smooth sidewalls (Song, 1994; Song & Chiew, 2001; Auel et al., 2014) (data as summarized in the tables of Guo (2015)). For nonuniform flows, the bed slope $\tan\alpha$ is corrected using equation (1b) of Guo (2015). The roughness sizes are $r=c_g/2$ for the experiments of Song (1994) (water-worked bed), $r=d_o$ for those of Song and Chiew (2001) (sand grains glued on aluminum plate), and r=k for those of Auel et al. (2014) (with k the measured absolute roughness).

Second, it is also consistent with experimental data from particle-free flows in open channels (b/h=2.94-7.79) consisting of rough beds and smooth sidewalls (Song, 1994; Song & Chiew, 2001; Auel et al., 2014) (figure 4B). As a side note, the strong quantitative difference between the spherical-grain data by Deal et al. (2023) and Ni and Capart (2018) discussed in the introduction (figure 1) is found to be predominantly the consequence of the latter authors' bed surface definition (NC18EXP* in figure 3D). In fact, figure 5 shows that the bed surface elevations resulting from their definition are much below ours. It can also be seen that the vertical profiles of the nondimensionalized local fluid shear stress Θ_{zx}^f for various flow strengths exhibit a focal point at the bed surface elevation (z=0) determined through our method, equation (7), with a focal value $\Theta_{zx}^f(0) \approx 0.04$ close to the transport threshold Shields number Θ_t . As discussed in §2.2, the occurrence of such a focal point constitutes a successful independent consistency check of equation (7).

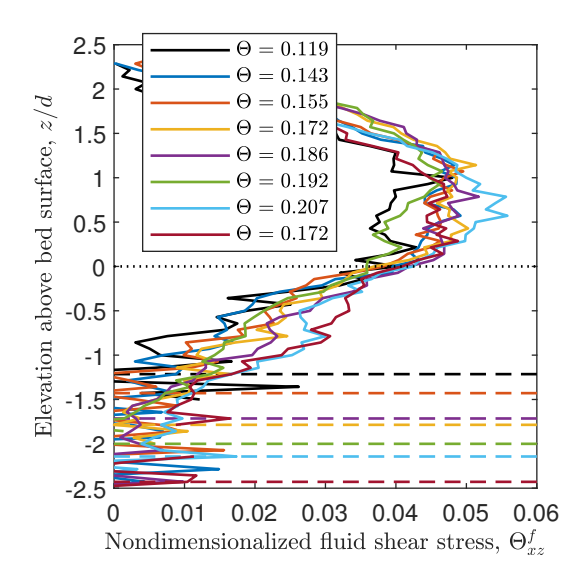


Figure 5. Independent evidence supporting our bed surface elevation definition. Vertical profiles (solid lines) of the nondimensionalized fluid shear stress $\Theta_{zx}^f \equiv \tau_{zx}^f/(\rho_p \tilde{g}_z d)$ for the data set NC18EXP (Ni & Capart, 2018). The data exhibit a focal point at the bed surface elevation z=0 defined by equation (7): $\Theta_{zx}^f(0)\approx 0.04$, a property required for Bagnoldian-type bedload models (Pähtz & Durán, 2018b). The fluid shear stress τ_{zx}^f is calculated from local quantities at the channel center as described in Chauchat (2018), assuming that the mixture viscosity obeys the closure measured by Boyer et al. (2011) for viscous suspensions. The dashed lines correspond to the bed surface elevations determined by Ni and Capart (2018).

3 Physical rough-bedload flux model across grain shapes, bed slopes, flow strengths and depths

In this section, we derive (§3.1) and validate (§3.3) a general bedload flux model. The validation makes use of an extended data compilation that complements the compilation for spherical grains, used in §2 to test channel geometry correction methods, with existing data from grain-shape-controlled experiments and grain-resolved CFD-DEM simulations for non-spherical grains, and with data for spherical and non-spherical grains from grain-unresolved CFD-DEM simulations (§3.2).

3.1 Model derivation

The model is derived in two steps. First, in §3.1.1, via generalizing an existing bed-load flux model (Pähtz & Durán, 2020), we obtain an expression that predicts the nondimensionalized bedload flux Q_* as a function of the excess Shields number $\Theta-\Theta_t$. Then, in §3.1.2, we explain how we calculate the unknown transport threshold Θ_t appearing in this expression.

3.1.1 Bedload flux

Using a numerical model coupling the Reynolds-averaged Navier-Stokes (RANS) equations with the DEM, Pähtz and Durán (2020) simulated non-suspended sediment transport of spherical grains and derived a general transport rate expression holding for a large range of conditions, including turbulent bedload with $s^{1/2}Ga \gtrsim 80$ and windblown sand:

$$Q_* = 2\kappa^{-1} \sqrt{\Theta_t} M_* (1 + c_M M_*), \tag{12}$$

with $M_* \equiv M/(\rho_p d)$. Based on the definition $M \equiv \rho_p h \langle \phi \rangle_z$ of the transport load in §2.1, M_* can be interpreted as a measure for the number N of transported grains above a bed surface area of size $\sim d^2$, that is, a particle activity (Ancey, 2020) or a height-averaged particle concentration. Furthermore, the term $c_M M_*$, with $c_M = 1.7$ a constant parameter determined from the simulations, encodes the rate of collisions between transported grains ($\propto M_*^2$) relative to that of grain-bed collisions ($\propto M_*^1$). In fact, equation (12) expresses the balance between global energy production due to drag (left-hand side) and energy dissipation due to grain contacts (right-hand side). In order to apply it to non-spherical grains, it is important to generalize d in a manner that retains $M_* \sim N$. Since grains transported at elevations close to the bed surface, where most transport takes place, tend to align their largest projected area A_p^{\max} parallel to the bed due to torque (Jain et al., 2020; Zhang et al., 2025), implying $M \sim N \rho_p V_p / A_p^{\max}$, this requirement begets $d \equiv \frac{3}{2} V_p / A_p^{\max}$. From approximating grains as ellipsoids, we estimate $V_p = \pi a_g b_g c_g / 6$ and $A_p^{\max} = \pi a_g b_g / 4$, leading to $d = c_g$ (already used in figure 4A).

In steady, homogeneous sediment transport, the average vertical force acting on transported grains is dominated by gravity, buoyancy, and potentially fluid lift, since drag forces during the grains' upward motion tend to cancel those during their downward motion (Pähtz & Durán, 2018a). When fluid lift is neglected, like in the simulations by Pähtz and Durán (2018b, 2020), this implies that the particle pressure at the bed surface $-\sigma_{zz}^p(0)$ is approximately equal to the submerged particle weight $M\tilde{g}_z$. The bed friction coefficient $\mu_b \equiv -\tau_{zx}^p(0)/\sigma_{zz}^p(0)$ then links $M\tilde{g}_z$ to the surface particle shear stress $\tau_{zx}^p(0)$. When further separating $\tau_{zx}^p(0)$ into gravity and drag contributions and assuming that particle drag on the fluid reduces the surface fluid shear stress $\tau_{zx}^f(0)$ to a value that is just sufficient to sustain transport, one obtains after some rearrangements Bagnold's (Bagnold, 1956) famous expression (Pähtz & Durán, 2018b)

$$M_* = \frac{\Theta - \Theta_t}{\mu_b - \tan \alpha},\tag{13}$$

which is a key ingredient of numerous bedload transport and windblown sand models in the literature, including the one by Pähtz and Durán (2020). Historically, it has been assumed that μ_b is equal to μ_s , the tangent of the static angle of repose of the bulk bed material (Bagnold, 1956). However, RANS-DEM simulations of turbulent bedload transport of spherical grains suggest that, although constant, μ_b is actually substantially larger than μ_s ($\mu_b \approx 0.7$ versus $\mu_s \approx 0.4$) (Pähtz & Durán, 2018b). This observation can be understood as a bed surface strengthening effect. Bedload transport increases the bed surface's ability to resist shear stress, since temporarily mobilized grains can settle again in more stable bed surface pockets (Clark et al., 2017). Whenever this happens, the bed surface becomes stronger relative to the bulk, i.e., $r_b \equiv \mu_b/\mu_s$ increases. This process continuous until a state is reached at which the pockets that emerge at the places where grains are mobilized are equivalent to the most stable pockets that transported grains can reach (Clark et al., 2017). Then, r_b has acquired its equilibrium value and will no longer increase. In viscous bedload, in which all pockets are reachable as a transported grain's kinetic energy is typically much smaller than the potential energy wells of the bed surface, $r_b \approx 3.4$ (Pähtz et al., 2021). However, in this study on turbulent bedload transport, where these two energy scales are of comparable size, r_b attains a smaller value as grains are too fast to probe the entire phase space of bed surface pockets (Clark et al., 2017). We use the value $r_b = 1.8$ suggested by the simulations $(1.8 \approx 0.7/0.4)$ of Pähtz and Durán (2018b) to calculate $\mu_b = r_b \mu_s$ from the measured μ_s .

In addition to using $\mu_b = r_b \mu_s$, we also generalize equation (13) to account for lift forces, defined as non-buoyancy fluid forces that act in the bed-normal direction. To this end, we note that equation (13) can be rearranged and brought into the form (Bagnold, 1956)

$$r_b \mu_s - \tan \alpha = \frac{\Theta - \Theta_t}{M_*} = \frac{M\overline{f_D}}{M\tilde{g}_z},$$
 (14)

in which $M\overline{f_D}$ represents the average streamwise drag force and $M\tilde{g}_z$ the average vertical submerged gravitational force acting on transported grains. The same kind of friction law, but generalized for the inclusion of lift forces, has also been derived when modeling incipient sediment motion (Wiberg & Smith, 1987). Denoting the average vertical lift force in the present context as $M\overline{f_L}$, the corresponding generalization of equation (14) transformed back to the form in equation (13) reads (Wiberg & Smith, 1987)

$$M_* = (\Theta - \Theta_t)/\mu^{\dagger}, \quad \text{with} \quad \mu^{\dagger} \equiv \frac{r_b \mu_s - \tan \alpha}{1 + r_b \mu_s \overline{f_L}/\overline{f_D}}.$$
 (15)

Note that, in Appendix C, we also straightforwardly derive equation (15) from the particle phase momentum balance via neglecting particle-sidewall interactions.

Equation (15) contains the single additional calibratable parameter $\overline{f_L}/\overline{f_D}$ and reduces to equation (13) if fluid lift is neglected. In real-world scenarios, one may expect $\overline{f_L}/\overline{f_D}$ to be of order unity, as suggested by measurements of drag and lift forces acting on surface roughness elements, including grains in bed surface pockets (Chepil, 1958, 1961). We use $\overline{f_L}/\overline{f_D} = 1.0$ because it optimizes the agreement between the final model and the entire data compilation.

3.1.2 Transport threshold

The prefactor $2\sqrt{\Theta_t}/\kappa$ in equation (12) resulted from interpreting Θ_t as the smallest Shields number that permits a quasi-continuous hopping-rebound motion (saltation) of a test grain in a grain-motion-undisturbed logarithmic fluid velocity profile (Pähtz & Durán, 2020). In such a scenario, lift forces acting on the moving test grain are typically much smaller than drag forces (Pähtz et al., 2021) due to the formers' rapid decrease with distance from the bed (Chepil, 1961). Then, it can be shown that, for conditions with $s^{1/4}Ga \gtrsim 200$, Θ_t in equation (12) obeys a scaling classically associated with the draginduced mobilization of a grain resting in a bed surface pocket (Pähtz et al., 2021):

$$\Theta_t = c_t (r_b \mu_s - \tan \alpha) / C_D, \tag{16}$$

where c_t is a dimensionless parameter and C_D an effective drag coefficient parametrizing the streamwise drag force acting on grains. It it smaller than that for settling grains, $C_{D\text{Settle}} = 4(s-1)gd/(3v_s^2)$ (Deal et al., 2023), where v_s is the terminal grain settling velocity, due to the smaller projected grain area exposed to the flow. Assuming again that transported grains tend to align their largest projected area $A_p^{\text{max}} = \pi a_g b_g/4$ parallel to the bed, the effective projected area A_p^{eff} in the streamwise direction is estimated as the geometric mean of the remaining two projected areas $\pi a_g c_g/4$ and $\pi b_g c_g/4$: $A_p^{\text{eff}} = \pi \sqrt{a_g b_g} c_g/4$, implying $A_p^{\text{eff}}/A_p^{\text{max}} = c_g/\sqrt{a_g b_g} \equiv S_f$, which is the Corey shape factor. Hence, we obtain $C_D = S_f C_{D\text{Settle}}$ or

$$C_D = 4S_f(s-1)gd/(3v_s^2). (17)$$

In the case of spherical grains, typical values for the quantities in equation (16) are $\mu_s \approx 0.46$, $C_D \approx 0.43$, and $\Theta_t \approx 0.05$ (Deal et al., 2023), implying $c_t \approx 0.03$. We use $c_t = 0.032$ because it optimizes the agreement between the final model and the entire data compilation. On the other hand, when $s^{1/4}Ga \lesssim 200$, viscous-sublayer effects render the scaling of Θ_t much more complicated (Pähtz et al., 2021). Therefore, we use equation (16) to determine Θ_t , except for the few numerical conditions with $s^{1/4}Ga < 200$ (BLRANSx in Table 1), for which we determine Θ_t directly from the simulations, as described by Pähtz and Durán (2020). Note that the data sets J21DNS and KU17DNS in Table 1, which also satisfy $s^{1/4}Ga < 200$, are excluded from this discussion as they violate the precondition $s^{1/2}Ga \gtrsim 80$ required for equation (12).

3.2 Extended data compilation

3.2.1 Experiments and grain-resolved CFD-DEM simulations

To evaluate our model, we require bedload flux data sets for shape-controlled grains, meaning they must provide the values of v_s and S_f , required to calculate C_D in equation (17), and the value of μ_s , which affects Q_* both via the calculation of M_* in equation (15) and via the calculation of Θ_t in equation (16). The data sets by Deal et al. (2023), denoted by D23EXPx in Table 1, where the 'x' stands for an arbitrary character, and by Zhang et al. (2022, 2025), denoted by Z22LESn, Z25LES, and Z22LESw in Table 1, satisfy this requirement. However, we excluded from Z25LES simulation data based on the "artificial-shrinkage method" by Zhang et al. (2025), since this method does probably not correspond to physically realistic scenarios (Chen et al., 2025). Furthermore, in order to use the spherical-grain data set NC18EXP by Ni and Capart (2018), who did not report μ_s , we acquired the same spheres from the same company and measured μ_s using the funnel method (Beakawi Al-Hashemi & Baghabra Al-Amoudi, 2018) in the manner described by Deal et al. (2023): by slowly pouring them onto an elevated disk bounded by a $2d_o$ -high rim (Appendix D). Moreover, we scoured the literature and found two more usable experimental data sets for non-spherical grains: the bedload flux measurements for cylinders (R22EXPc) and lenses (R22EXPl) by Rebai et al. (2022). For both grain shapes, v_s (Matoušek & Zrostlík, 2020) and the grain dimensions (required for S_f) have been reported, while μ_s was measured using the funnel method in a box filled with water, which was sufficiently large to rule out potential box-sidewall friction effects (private correspondence with the authors). We confirmed with DEM simulations that different procedures of conducting the funnel method have only a small effect on μ_s (< 5%) provided that a sufficiently large number of grains is used and that there is some means of preventing grains from rolling away (such as a rim or rough bed, see Appendix D).

For those data sets mentioned in the previous paragraph that were not already discussed in §2.4.1 on the spherical-grain data compilation, we determine the bed surface elevation using the method described in §2.2, provided the required data are available from the studies. This is the case for the data set R22EXPl (figure 6A). Note that, for

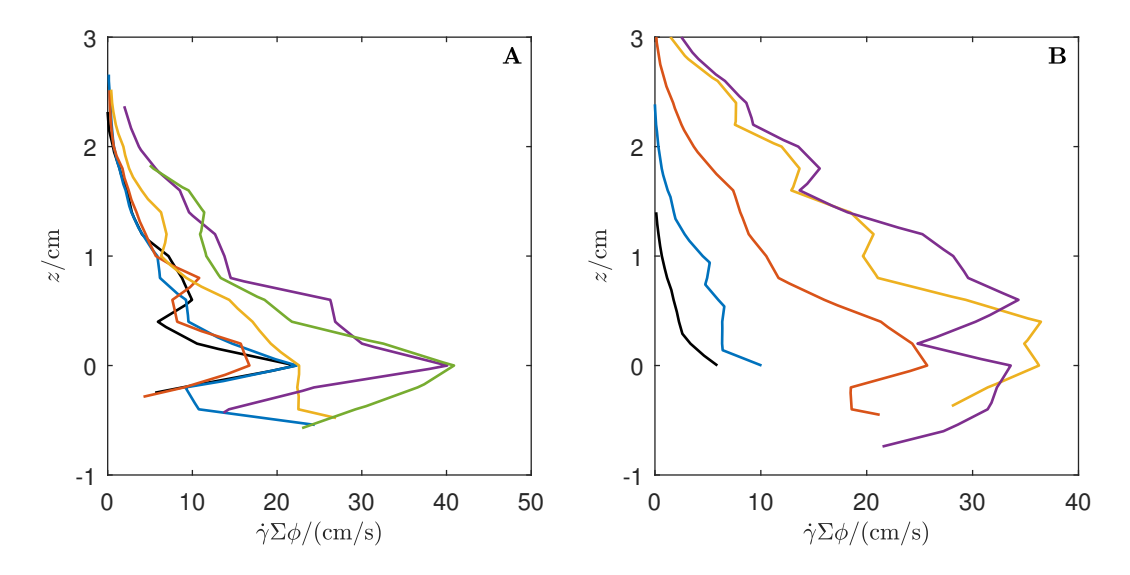


Figure 6. Determination of bed surface elevation for experimental data sets R22EXPl and R22EXPc (Rebai et al., 2022). Vertical profiles of $\dot{\gamma}\Sigma\phi$. The data in A are used to determine the bed surface elevation, whereas the data in B are not sufficiently highly resolved to discern a maximum of $\dot{\gamma}\Sigma\phi$.

R22EXPl, the ratio $R_h^l \equiv h/h^{\rm R22l}$ between h, estimated using our method, and the value $h^{\rm R22l}$ reported by Rebai et al. (2022) varies between 0.91 and 1.02. However, for the data set R22EXPc, the reported vertical profiles of $\Sigma \phi$ are not sufficiently highly resolved to determine h (figure 6B), and we therefore use reported values $h^{\rm R22c}$ multiplied by the average of R_h^l from the R22EXPl data set. Furthermore, since the data required to determine h from our method are not available for D23EXPx and Z25LES, we use the values of h reported in the respective studies, as justified by $h^* = h/d \gg 1$ (Table 1). For more details and the calculation of the bed shear stress uncertainty, see Appendix B.

3.2.2 Grain-unresolved CFD-DEM simulations

Since our bedload flux model generalizes equation (13), the transport load expression by Bagnold (1956), to equation (15), involving the additional parameter $\overline{f_L/f_D}$ 1.0, we test it also for conditions to which equation (13) applies (i.e., $\overline{f_L}/\overline{f_D} = 0$). For this purpose, we add data from grain-unresolved CFD-DEM simulations to the compilation, both from existing studies (Pähtz & Durán, 2020; Maurin et al., 2018; Monthiller, 2019) and from our simulations, all of which were conducted using either of the numerical models described by Durán et al. (2012), Maurin et al. (2015), or Xie et al. (2022) (Table 1, for details see Appendix E). They differ from grain-resolved simulations in the fact that they do not resolve the flow around single grains, and they therefore incorporate empirical relations for the buoyancy, drag, and lift forces acting on grains, the latter of which are typically neglected (also here, i.e., $\overline{f_L}/\overline{f_D} = 0$). They also allow us to perform thought experiments in which C_D is treated as just another control parameter, since we can artificially modify C_D through changing the drag force parameters (Appendix E), see LESCD and BLRANSCD in Table 1. Another purpose of adding these data is to confront our bedload flux model with transport conditions across a much larger range of the control parameters Θ , α , and h^* than that spanned by the experiments and grainresolved simulations alone.

3.2.2.1 Streamwise momentum balance in BLRANSx The numerical model of Durán et al. (2012) behind the data sets BLRANSx considers a flow in an inner turbulent boundary layer of infinite height (no sidewalls). To be consistent with equation (5), we slightly modified the streamwise fluid momentum balance employed by Durán et al. (2012) to

$$d_z \tau_{zx}^f = \rho_f \phi g \sin \alpha + \rho_p \phi f_x^{f \to p}, \quad \text{with} \quad \tau_{zx}^f(\infty) = \tau_b,$$
 (18)

before conducting simulations, where $\rho_p \phi f^{f \to p}$ is the fluid-particle interaction force per unit volume of the mixture. In fact, integrating equation (18) from zero to infinity and combining the result with equation (C5) and $\tau_{zx}(0) = \tau_{zx}^f(0) + \tau_{zx}^p(0)$ leads precisely to equation (5). Note that, for the numerical model of Durán et al. (2012), the Shields number $\Theta \equiv \tau_b/(\rho_p \tilde{g}_z d)$ based on τ_b in equation (18) is a prescribed fixed parameter.

3.2.2.2 Determination of Θ for M18RANS, M19RANSx, and LESx. Since the raw data required to determine the bed surface elevation, and thus h and τ_b , are not available for the data sets M18RANS (Maurin et al., 2018) and M19RANSx (Monthiller, 2019) in Table 1, based on the model by Maurin et al. (2015), we below derive the relationship between their reported transport-driving Shields number Θ_* and our Shields number Θ .

Maurin et al. (2015) defined $\Theta_* \equiv \tau_{\rm cl}/(\rho_p \tilde{g}_z d)$ as the Shields number based on the clear-water fluid shear stress $\tau_{\rm cl}$ on the top of the bedload layer:

$$\tau_{\rm cl} \equiv \max \tau_{zx}^f(z). \tag{19}$$

Using $\tau_b \propto h$ for their sidewall-free channels, $\tau_{\rm cl}$ therefore defines an effective clear-flow depth as

$$h_{\rm cl} \equiv h \tau_{\rm cl} / \tau_b \tag{20}$$

and subsequently an effective bedload layer thickness above the bed surface as

$$h_p \equiv h - h_{\rm cl}. \tag{21}$$

The latter is linked to the transport load M via

$$M = \rho_p h_p \phi, \tag{22}$$

with $\underline{\phi} \equiv \frac{1}{h_p} \int_0^h \cdot \mathrm{d}z \approx \frac{1}{h_p} \int_0^{h_p} \phi \mathrm{d}z$ the approximate average of the particle volume fraction $\overline{\phi}$ over the bedload layer thickness. Combining the above relations and nondimensionalizing the result yields

 $\Theta = \Theta_* \left(1 + \frac{M_*}{\phi h_{\rm cl}^*} \right), \tag{23}$

where $h_{\rm cl}^* \equiv h_{\rm cl}/d$ is the dimensionless clear-flow depth.

To determine the parameter $\underline{\phi}$ in equation (23), we combine equation (23) with equation (13), valid for the grain-unresolved simulations due to $\overline{f_L}/\overline{f_D} = 0$, yielding

$$\underline{\phi} = J \left(1 - \frac{\Theta_* - \Theta_t}{(r_b \mu_s - \tan \alpha) M_*} \right)^{-1}, \tag{24}$$

with $J \equiv \Theta_*/[h_{\rm cl}^*(r_b\mu_s - \tan\alpha)]$. The unknown values of M_* in equation (24) can be estimated from the simulation data of Q_* via equation (12), using the predicted values of Θ_t from equation (16). Figure 7 shows the resulting *estimates* of ϕ as a function of J for the grain-unresolved data sets M18RANS, M19RANSx, LES, and LESCD. Note

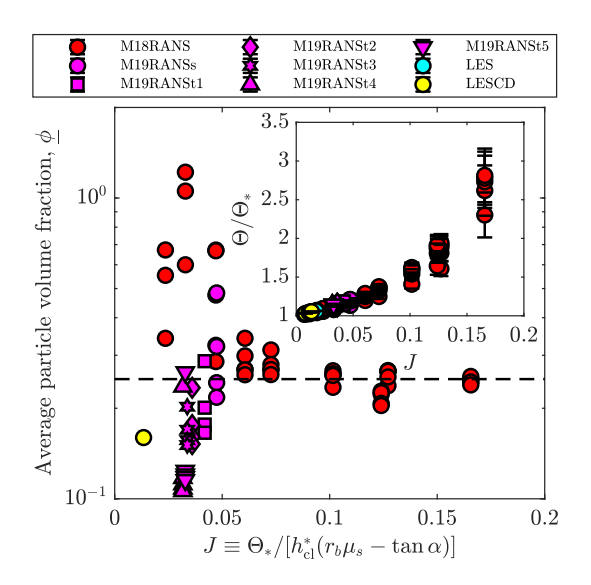


Figure 7. Determination of transport-layer-averaged particle volume fraction $\underline{\phi}$. $\underline{\phi}$, estimated from the Q_* -data as described in the text, versus J. Symbols correspond to grain-unresolved CFD-DEM simulations (Table 1). The dashed line indicates the value $\underline{\phi}=0.25$ exhibited for large J, where the ratio Θ/Θ_* deviates from unity the most. Inset: Estimate of Θ/Θ_* resulting from $\underline{\phi}=0.25$, where the error bars correspond to the propagated uncertainty of μ_s , required for predicting M_* and therefore Θ , as described in the text.

that the estimates for $J \lesssim 0.05$ cannot be trusted, since they are very sensitive to even slight variations in the simulation data of Θ_* , $h_{\rm cl}^*$, and especially Q_* , explaining the large scatter and the occasionally unphysically large values of ϕ for low J. However, this is

not a serious issue, since for weak transport conditions, Θ_* is close to Θ no matter the precise value of $\underline{\phi}$ as M_* in equation (23) becomes small. In contrast, for $J\gtrsim 0.05$, the estimations of $\underline{\phi}$ from the simulation data scatter relatively little between only about 0.2 and 0.3 (figure 7). In particular, for the most intense conditions, $\underline{\phi}\approx 0.25$, which is a reasonable value as it is about half of $\phi(0)$ for intense transport conditions (Pähtz & Durán, 2018b). We therefore fix $\underline{\phi}=0.25$ in equation (23) as a simple means to relate Θ to Θ_* for arbitrary conditions through equation (23). The ratio Θ/Θ_* resulting from this choice is shown in the inset of figure 7.

Although we have used the M_* -values estimated from the Q_* -data via equation (12) to obtain $\phi = 0.25$, we do not do so when estimating Θ from equation (23), in order to avoid an implicit dependence of Θ on Q_* . Instead, we obtain Θ from the values of M_* predicted by equation (15). The uncertainty of Θ in the upcoming figures then corresponds to the propagated uncertainty of μ_s in the calculation of Θ via equations (15) and (23).

3.2.2.3 Streamwise buoyancy force in M18RANS and M19RANSx Some of the existing grain-unresolved simulations (M18RANS and M19RANSx in Table 1) neglected streamwise buoyancy forces following the assumption that Reynolds and other shear stresses do not contribute to buoyancy (Maurin et al., 2018; Pähtz et al., 2021). However, this assumption was very recently shown to be false (Rui et al., 2025). To adjust for this mistake, we use a modification of equation (16) in which $\tan \alpha$ is replaced by $(1-1/s)^{-1} \tan \alpha$ for these simulations, resulting in the expression one would expect in the absence of streamwise buoyancy forces. In contrast, equation (13), valid for M18RANS and M19RANSx due to $\overline{f_L}/\overline{f_D} = 0$, does not change when streamwise buoyancy forces are neglected (Pähtz et al., 2021).

3.3 Model validation

As a result of the wide range of control parameters and methods, the data of Q_* from the grain-unresolved simulations alone, and in extension from the entire data compilation, can vary by almost an order of magnitude at a given Θ (figure 8). Nonetheless, the predictions from our bedload flux model deviate by less than a factor of 1.3 from almost all these data (figure 9). As a side note, this does not only constitute a validation of our bedload flux model but also lends support to the reliability of the grain-unresolved simulations, since, if these were obeying different physics, one would not expect them to be captured by the same physical analytical model.

4 Discussion

4.1 The role of fluid lift in bedload transport

Our rough-bedload flux model combines the global energy balance, equation (12) after Pähtz and Durán (2020), linking the bedload flux to the transport load, with Bagnold's (Bagnold, 1956) famous transport load expression, equation (15), generalized to account for a non-vanishing ratio $\overline{f_L}/\overline{f_D}$ between the average lift and drag forces acting on transported grains. This is curious in so far as fluid lift is often assumed to be negligible in bulk bedload transport (Pähtz & Durán, 2020; Pähtz et al., 2021; Deal et al., 2023), mainly because once grains detach from the bed, the shear-induced lift force acting on them rapidly declines with elevation (Chepil, 1961) and may even become negative (Li et al., 2019; Shi & Rzehak, 2019). In this regard, it is also interesting that $\overline{f_L}/\overline{f_D}$ has no bearing on the transport threshold Θ_t in equation (16). (We confirmed that including $\overline{f_L}/\overline{f_D}$ in equation (16) in a fashion after Wiberg and Smith (1987) results in failure of the overall model.) The key difference between equation (15) and equation (16) is that the former is associated with liquid-like bulk bedload transport, in which many grains are in a rolling mode even for weak transport conditions (Benavides et al., 2023),

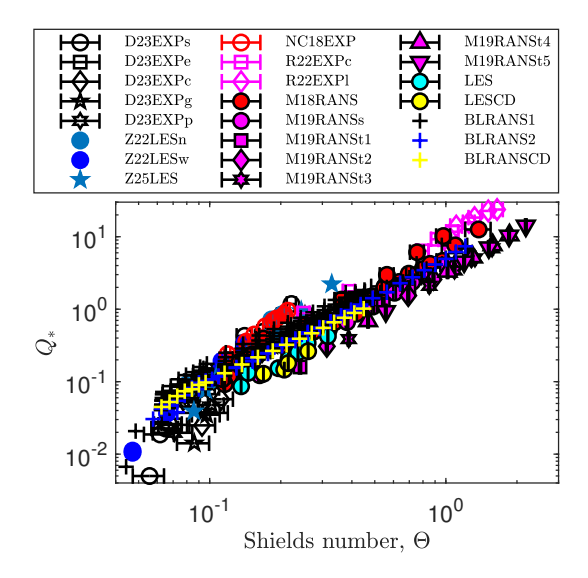


Figure 8. Entire data compilation. Nondimensionalized bedload flux Q_* versus Shields number Θ , both rescaled using the generalized grain diameter definition $d \equiv \frac{3}{2}V_p/A_p^{\max}$ (see text). Symbols correspond to data from a variety of experimental and numerical methods (Table 1). An error bar indicates the standard error and/or uncertainty range. In the absence of error bars, uncertainties are smaller than the symbol size.

whereas the latter is obtained from a theoretical picture in which a single test grain continuously hops along the bed surface (i.e., a gas-like granular flow). This hints on the possibility that collectively rolling grains somehow cause the emergence of substantial fluid lift in bulk bedload transport. For example, one might speculate that, in contrast to grains at rest, such grains are exposed to lifting lubrication forces, which are known as the primary agent controlling the rheology of viscous sediment transport (Vowinckel et al., 2021). In this regard, it is curious that the only data set deviating from the sphericalgrain collapse in figure 3D is KU17DNS, based on a DNS-DEM code that does not include a correction for short-range lubrication forces that is arguably required when the distance between two approaching grains falls below one DNS grid length (Biegert et al., 2017). In addition, unlike the numerical models behind the other grain-resolved simulations in figure 3D, the model by Kidanemariam and Uhlmann (2017) behind KU17DNS has not been explicitly shown to reproduce lubrication-distorted grain trajectories. Although we attributed the deviation of KU17DNS from the data collapse to a smooth transport regime due to the comparably small Galileo numbers Ga in these simulations, it is also possible that the actual reason might be their lacking correction for short-range lubrication. This speculation would also be consistent with the fact that KU17DNS exhibits essentially the same bedload flux curve as the grain-unresolved spherical-grain simulation data sets (not shown), for which $\overline{f_L}/\overline{f_D} = 0$ by definition. However, exploring this or alternative speculations requires further study in the future.

4.2 Test of Deal et al.'s rough-bedload flux model with independent data

We are only aware of a single alternative bedload flux model attempting to account for grain shape: the one by Deal et al. (2023). These authors generalized d to the volume-equivalent sphere diameter d_o , as opposed to the shortest grain axis c_g in our model, and used the modified Shield number $\Theta^{D23} \equiv \tau_b/(\rho_p \tilde{g}_z d_o)$ and modified nondimensionalized bedload flux $Q_s^{D23} \equiv Q/(\rho_p d_o \sqrt{(s-1)gd_o})$ to quantify the flow strength and transport rate, respectively. They proposed that bedload flux data corresponding to differ-

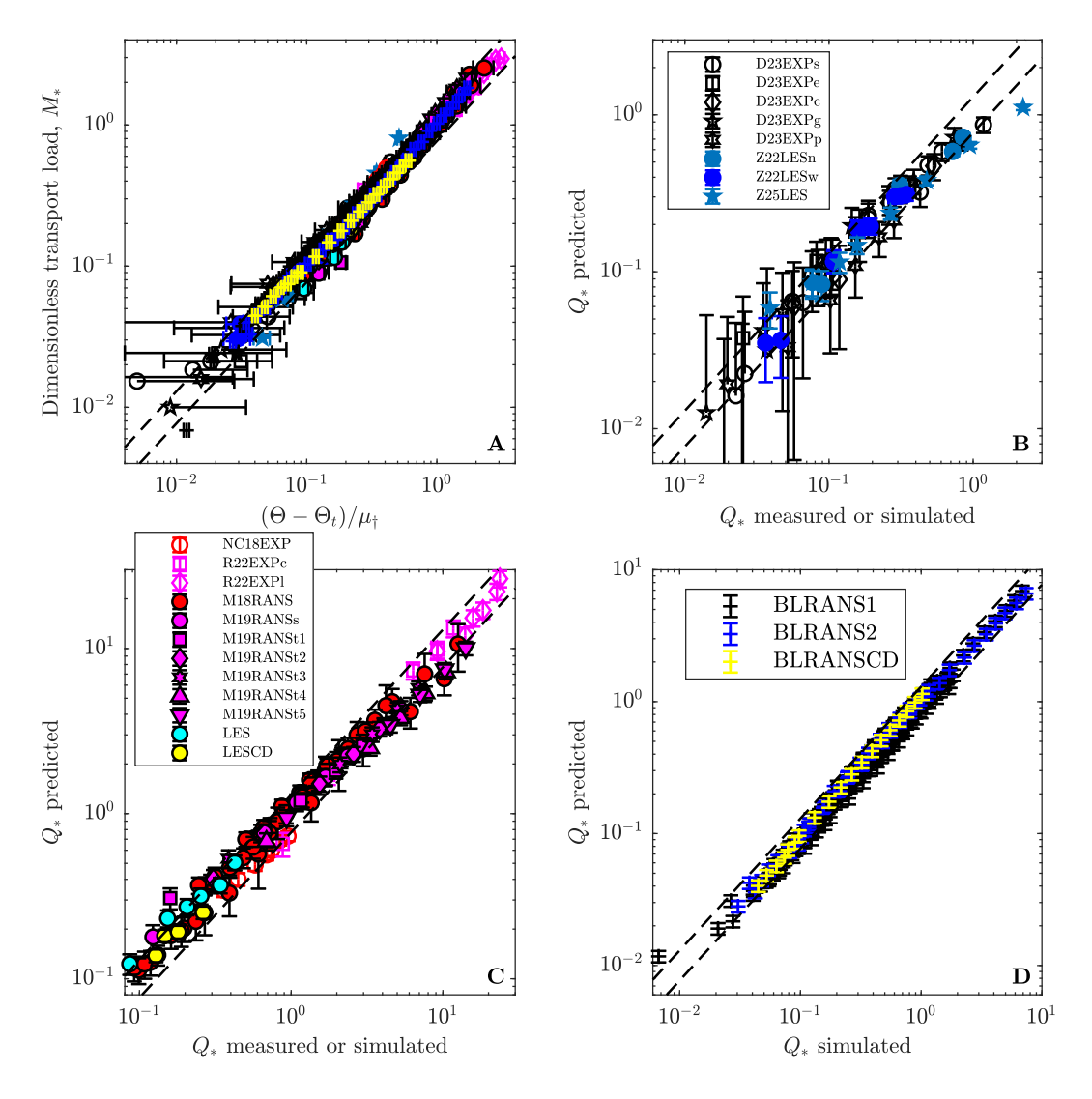


Figure 9. Test of our rough-bedload flux model across grain shapes, bed slopes, flow strengths, and flow depths. (A) Nondimensionalized transport load M_* , calculated from the Q_* -data via equation (12), versus ($\Theta - \Theta_t$)/ μ_{\uparrow} . (B-D) Q_* predicted by equations (12) and (15) versus measured or simulated Q_* . Symbols correspond to data from a variety of methods (Table 1). An error bar indicates the standard error and/or uncertainty range. In the absence of error bars, uncertainties are smaller than the symbol size. When $s^{1/4}Ga \geq 200$, Θ_t is calculated by equation (16). Otherwise (only BLRANSx), Θ_t is determined directly from the simulations, as described in Pähtz and Durán (2020). All grain-unresolved simulations neglect lift forces, implying $\overline{f_L}/\overline{f_D} = 0$. Almost all data fall within a factor of 1.3 of the model prediction, delineated by the dashed lines.

ent grain shapes collapse onto a single curve $Q_*^{\mathrm{D23}} = f[(C^*/\mu^*)\Theta^{\mathrm{D23}}]$, where C^* is the sphere-normalized value of $C_D d_o/c_g$ (Appendix F) and $\mu^* \equiv (\mu_s - \tan \alpha)/(\mu_o - \tan \alpha)$, with $\mu_o = \tan 24^\circ$ the approximate value of μ_s for spheres.

Deal et al. (2023) validated their model with their bedload flux measurements for several grain shapes, but not with other experimental data from independent sources. Here, we test their model with the independent data sets from our data compilation, sidewall-

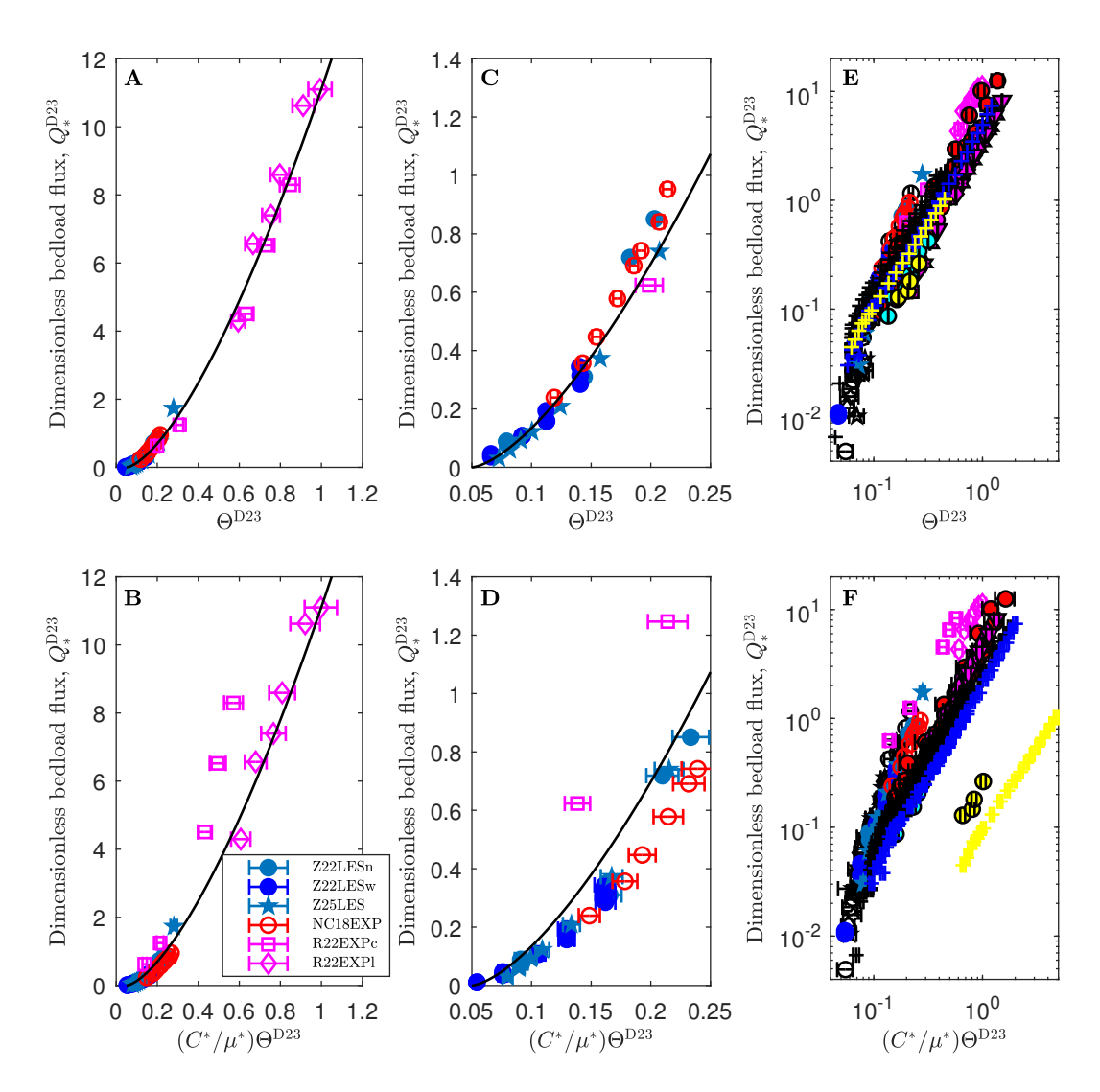


Figure 10. Test of bedload flux model of Deal et al. (2023) with independent data. Nondimensionalized bedload flux $Q_*^{\rm D23}$ versus shape-uncorrected Shields number $\Theta^{\rm D23}$ (A, C, E) and shape-corrected Shields number $(C^*/\mu^*)\Theta^{\rm D23}$ (B, D, F), based on the same definitions as Deal et al. (2023). Symbols in (A-D) correspond to data from experiments and grain-resolved simulations from independent studies (Table 1). Symbols in (E, F) correspond to the entire data compilation, including D23EXPx (Deal et al., 2023) and data from grain-unresolved simulations. An error bar indicates the standard error and/or uncertainty range. In the absence of error bars, uncertainties are smaller than the symbol size. The solid lines correspond to $Q_*^{\rm D23} = 12(\Theta^{\rm D23} - 0.05)^{3/2}$ (A, C) and $Q_*^{\rm D23} = 12(\Theta^{\rm D23}C^*/\mu^* - 0.05)^{3/2}$ (B, D). The latter is the prediction by Deal et al. (2023).

corrected with our derived universal method (figure 10). We remind the reader that, when applied to the data sets by Deal et al. (2023), this correction yields almost the same bed shear stress τ_b as their own empirical correction (figure 4A), while unifying spherical-grain data sets across experimental facilities (figure 3D). So, any unfavorable outcome of this test is likely not attributable to the application of our method. To be as fair as possible, we focus on those independent data sets obtained from experiments and grain-resolved simulations (figures 10A-10D) and use the entire data compilation only as a secondary

addition to our arguments (figures 10E and 10F). It can be seen that the grain shape correction by Deal et al. (2023) (figures 10B and 10D) much increases the scatter in the independent data when compared with the situation without correction (figures 10A and 10C), both for intense and weak transport conditions. In particular, the chosen range 0.05-0.25 of the (un)corrected Shields number in figures 10C and 10D is equivalent to the range of their own experiments (Deal et al., 2023), and the maximum scatter in figure 10D by more than a factor of 3 occurs well within this range, at $(C^*/\mu^*)\Theta^{D23}\approx 0.14$. It is caused by the data set R22EXPc in Table 1, for which $C^*/\mu^*=0.69$, a more extreme value of C^*/μ^* than in all their experiments $(C^*/\mu^*=0.84-1.05)$ (Deal et al., 2023). Note that, even if we used the water depths h^{R221} reported by Rebai et al. (2022) to obtain τ_b and subsequently Θ , which are very slightly (4%) larger than the values h we estimated, the strong disagreement between the data set R22EXPc and the model by Deal et al. (2023) would remain.

We believe that this poor performance chiefly results from their incorporation of C^* in their grain shape correction of the Shields number. In fact, it was shown that models that express bedload flux as a function of the excess bed shear stress are inherently linked to the assumption by Bagnold (1956), later confirmed (Pähtz & Durán, 2018b), that the bed friction coefficient μ_b is constant. (In the model of Deal et al. (2023), $\mu_b =$ μ_s , whereas $\mu_b = r_b \mu_s$ in our model.) In equilibrium, this constant friction coefficient is equal to the ratio between the average streamwise and normal-bed forces acting on transported grains, rendering the average drag force per unit mass $\overline{f_D}$ insensitive to the details of the flow. In consequence, increments of C^* (or C_D in our model) tend to be compensated by decrements of the average fluid-particle velocity difference, keeping $\overline{f_D}$ and therefore the effective transport-driving shear stress constant. Note that this reasoning is corroborated by the fact that the yellow symbols in figures 10E and 10F, corresponding to conditions with artificially strongly elevated values of C^* or C_D (LESCD) and BLRANSCD in Table 1), shift far away from the rest of the data after employing the grain shape correction by Deal et al. (2023). In contrast, they are captured by our bedload flux model (figure 9D) because it does not modify the Shields number Θ by a drag-dependent correction.

5 Conclusions

We have derived a universal channel geometry correction method to determine the bed shear stress that collapses spherical-grain data of the nondimensionalized bedload flux Q_* as a function of the Shields number Θ (figure 3), obtained from experiments and grain-resolved CFD-DEM simulations, across a wide range of geometries, including narrow-deep and wide-shallow open channel flows. It consists of a physically-based method to determine the bed surface elevation and a sidewall correction derived from Kolmogórov's theory of turbulence. The latter incorporates a single parameter ($c_{bw} = 2.23$ in equation (10)) that is exclusively related to approximately channel-geometry-independent scaling coefficients in that theory. We have applied the channel geometry correction method to a very diverse compilation of grain-shape-controlled data sets from experiments, grain-resolved, and grain-unresolved CFD-DEM simulations (Table 1). An existing bedload flux model, here generalized to account for grain shape variability, predicts almost all these data within a factor of 1.3 (figure 9). In contrast, the only, to our knowledge, existing alternative bedload model accounting for grain shape variations (Deal et al., 2023) clearly disagrees with the data compilation (figure 10).

In view of the diversity of the data compilation in terms of sediment transport and channel flow conditions, and the methods it is based on, the degree by which our relatively simple model, with only three adjustable parameters, agrees with it is remarkable (figure 9). It suggests that, with the here employed sidewall correction and bed surface definition, and our physical model to predict the flux of rough bedload transport (applicable if $s^{1/2}Ga \gtrsim 80$, satisfied for most conditions in nature), bedload variability is

largely diminished, at least for the idealized case considered here (steady flows over flat beds at short timescales). This is a prerequisite for discerning different sources of variability in the more complex situations typically encountered in nature.

6 Open Research Section

The data required to reproduce figures 3, 4A, and 7-10, and a MATLAB code to plot them are available online at https://zenodo.org/records/17556370. The measurements of μ_s resulting from the experiment in figure D1 and simulations in figure D2 are reported in Table 1. The data plotted in figure 4B are from the tables of Guo (2015). The data plotted in figure 1 are from Ni and Capart (2018) and Deal et al. (2023) and can also be plotted using the MATLAB code. The data plotted in figures 2 and 5 are from the supplementary materials of Ni and Capart (2018). The data plotted in figures 6A and 6B are from the tables and supplementary materials of Rebai et al. (2022). All data needed to evaluate the conclusions of the paper are present in the paper.

Acknowledgments

Z.H. acknowledges financial support from grant National Key R & D Program of China (2023YFC3008100). T.P. acknowledges financial support from grants National Natural Science Foundation of China (nos. 12350710176, 12272344). O.D. acknowledges financial support from Texas A&M Engineering Experiment Station. The authors thank Yesheng Lu for helping finding grain-shape-controlled bedload transport data sets.

Appendix A Einstein-Johnson's sidewall correction

The empirical sidewall correction by Einstein-Johnson calculates the friction factor ratio f_w/f_b in equation (8) as (Guo, 2017)

$$f_w/f_b = R_w/R_b$$
, with $R_b = (1 - 2R_w/b)$, $R_w = f^{-1}R[6\log_{10}[W(x)/x]]^{-2}$, $f = 8U^{-2}gR\sin\alpha$, $x = [9\Re/(100f)]^{1/3}$, (A1)

where W(x) denotes the principal branch of the Lambert W function. These expressions constitute an analytical solution of the system of equations by Einstein (1942) and Johnson (1942), improving their iterative solution method as well as the graphical approximation by Vanoni and Brooks (1957).

Appendix B Estimation of bed shear stress and its uncertainty

B1 NC18EXP

For this highly-resolved data set, the profiles of $\dot{\gamma}\Sigma\phi$ exhibit several local maximums due to layering (figure 2). We choose the top-most local maximum at the bed surface elevation, defined in equation (7), because the profiles $\Theta^f_{zx}(z)$ exhibit a focal point there, with $\Theta^f_{zx}(0)\approx\Theta_t$ (figure 5), consistent with the theoretical expectation (Pähtz & Durán, 2018b). It occurs $\Delta z=31.75\pm0.5$ mm above the channel bottom for all flow conditions. The upper and lower bounds $\Delta z=32.25$ mm and $\Delta z=31.25$ mm then yield corresponding lower (h_{\min}) and upper (h_{\max}) bounds, respectively, of h for a given flow condition, with corresponding bed shear stress estimates $\tilde{\tau}_b(h_{\max})$ and $\tilde{\tau}_b(h_{\min})$, respectively, obtained from equations (8) and (10). Hence, we estimate τ_b and its uncertainty as

$$\tau_b = \frac{1}{2} \left[\tilde{\tau}_b(h_{\text{max}}) + \tilde{\tau}_b(h_{\text{min}}) \right] \pm \frac{1}{2} \left[\tilde{\tau}_b(h_{\text{max}}) - \tilde{\tau}_b(h_{\text{min}}) \right], \tag{B1}$$

B2 R22EXPx

Two data sets are reported: one for grains with lens shape (R22EXPl) and one for cylindrical grains (R22EXPc). Since the authors' experimental methods did not resolve $v_x(z)$ inside the sediment bed (Rebai et al., 2022) and due to an insufficient data resolution for reliably calculating velocity gradients, the vertical profiles of $\dot{\gamma}\Sigma\phi$ are of a rather poor quality near the bed (figures 6A and 6B), with some of the cylinder data not even exhibiting a pronounced maximum of $\dot{\gamma}\Sigma\phi$. For R22EXPl, we determine h from the most pronounced maximum and calculate the ratio $R_h^1 \equiv h/h^{\text{R22l}}$, where h^{R22l} is the reported flow depth value. It was measured as the depth over the mean of (i) the elevation at which the linear extrapolation of $v_x(z)$ vanishes and (ii) the interpolated elevation at which the particle volume fraction $\phi = 0.6$ (Rebai et al., 2022). Since this method requires neither particle velocity data inside the sediment bed nor calculating particle velocity gradients, h^{R22l} , and its counterpart h^{R22c} for R22EXPc, is more much precisely determinable than h. The value of R_h^l varies little with flow conditions, between about $\min(R_h^l) =$ 0.91 and $\max(R_h^l) = 1.02$. Assuming that, under hypothetically experimentally ideal conditions, R_h^l does not depend on the sediment transport condition, we use it to obtain τ_b and its uncertainty range from the estimate $\tilde{\tau}_b^{R22} \equiv \tilde{\tau}_b(h^{R22})$, obtained from equations (8) and (10), for both R22EXPl and R22EXPc as follows:

$$\tau_b = \frac{1}{2} \left[\max(R_h^{\rm l}) + \min(R_h^{\rm l}) \right] \tilde{\tau}_b^{\rm R22} \pm \frac{1}{2} \left[\max(R_h^{\rm l}) - \min(R_h^{\rm l}) \right] \tilde{\tau}_b^{\rm R22}, \tag{B2}$$

where $h^{\rm R22}$ in the definition of $\tilde{\tau}_b^{\rm R22}$ stands representative for either $h^{\rm R22l}$ or $h^{\rm R22c}$.

B3 Z22LESw

The values of h^* reported for this data set are based on equation (7) (Zhang et al., 2022). We therefore use the reported values of h^* and Θ , assuming that the uncertainty of Θ is very small (smaller than the respective symbols in the plots).

B4 D23EXPx, Z22LESn, and Z25LES

For these data sets, we use the reported values of h as its effect on τ_b is very small because of very small width-to-depth ratios $(b/h\approx 0.1)$ and because h was much larger than the bedload layer thickness (Deal et al., 2023; Zhang et al., 2022, 2025). For the numerical data sets Z22LESn and Z25LES, we therefore conclude that the uncertainty of τ_b is very small (smaller than the respective symbols in the plots). For the experimental data sets D23EXPx, the main source of uncertainty comes from the determination of the bed slope angle α . We propagate its reported uncertainty to estimate the uncertainty of τ_b .

B5 J21DNS and KU17DNS

As we do not have access to the raw data of these data sets, and since h was much larger than the bedload thickness (Jain et al., 2021; Kidanemariam & Uhlmann, 2017), we use the reported values of h^* and Θ , assuming that the uncertainty of Θ is very small (smaller than the respective symbols in the plots).

B6 M18RANS, M19RANSx, LESx

For these data sets, see §3.2.

B7 BLRANSx

For these data sets, $h^* = \infty$ by construction and Θ is a prescribed parameter (no uncertainty, see §3.2).

Appendix C Transport load expression

To derive simple expressions for the dimensionless transport load M_* , we henceforth neglect the contributions of particle-sidewall interactions in the streamwise and vertical particle momentum balances. Then, these balances read (Pähtz et al., 2025)

$$d_z \tau_{zx}^p = -\rho_p \phi g \sin \alpha - \rho_p \phi f_x^{f \to p}, \tag{C1}$$

$$d_z \sigma_{zz}^p = \rho_p \phi g \cos \alpha - \rho_p \phi f_z^{f \to p}, \tag{C2}$$

where $\rho_p \phi \mathbf{f}^{f \to p}$ is the fluid-particle interaction force per unit volume of the mixture. In both balance equations, we decompose $\rho_p \phi \mathbf{f}^{f \to p}$ into buoyancy and non-buoyancy contributions. The latter are identified as the drag $(\rho_p \phi \tilde{f}_D)$ and lift $(\rho_p \phi \tilde{f}_L)$ forces per unit volume of the mixture for the streamwise and vertical directions, respectively. We model this force decomposition following a recent discovery regarding the nature of the buoyancy force in dynamic systems (Rui et al., 2025):

$$f_D \equiv \frac{\tilde{f}_D}{1 - \phi} = \tilde{f}_D + \frac{\phi \tilde{f}_D}{1 - \phi} = f_x^{f \to p} + s^{-1}g \sin \alpha, \tag{C3}$$

$$f_L \equiv \frac{\tilde{f}_L}{1 - \phi} = \tilde{f}_L + \frac{\phi \tilde{f}_L}{1 - \phi} = f_z^{f \to p} - s^{-1} g \cos \alpha, \tag{C4}$$

In equations (C3) and (C4), buoyancy force contributions originating from drag $(\rho_p \phi \tilde{f}_D/(1-\phi))$ and lift $(\rho_p \phi \tilde{f}_L/(1-\phi))$ have been lumped into $\rho_p \phi f_D$ and $\rho_p \phi f_L$, which represent the drag and lift forces, respectively, per unit volume of pure fluid. Using equations (C3) and (C4), integration of equations (C1) and (C2), respectively, yields

$$\tau_{zx}^{p}(0) = M\left(\tilde{g}_z \tan \alpha + \overline{f_D}\right),\tag{C5}$$

$$\sigma_{zz}^{p}(0) = -M\left(\tilde{g}_z - \overline{f_L}\right). \tag{C6}$$

It follows that the bed friction coefficient, $\mu_b \equiv -\tau_{zx}^p(0)/\sigma_{zz}^p(0)$, constrains the average forces acting on transported grains:

$$\mu_b = \frac{\tilde{g}_z \tan \alpha + \overline{f_D}}{\tilde{g}_z - \overline{f_L}}.$$
 (C7)

This equation can be transformed into

$$\mu_{\dagger} \equiv \frac{\overline{f_D}}{\tilde{g}_z} = \frac{\mu_b - \tan \alpha}{1 + \mu_b \overline{f_L} / \overline{f_D}}.$$
 (C8)

Finally, combining equations (C5) and (C8) with equation (5) and $\tau_{zx} = \tau_{zx}^f + \tau_{zx}^p$, nondimensionalizing, and employing $\Theta - \Theta_{zx}^f(0) \equiv (\tau_b - \tau_{zx}^f(0))/(\rho_p \tilde{g}_z d) = \Theta - \Theta_t$ (Pähtz & Durán, 2018b) leads to equation (15).

Appendix D Determinations of angle of repose and its uncertainty

We acquired the same spheres as those used in Ni and Capart (2018) (NC18EXP in Table 1) from the same company (Chiao Dar Acry & Advertisement Co., Ltd., http://www.bridgeacry.com.tw http://www.bridgeacry.com.tw) and measured μ_s using the funnel method (Beakawi Al-Hashemi & Baghabra Al-Amoudi, 2018) in the manner described in Deal et al. (2023) (figure D1). Furthermore, we confirmed with DEM simulations that different measurement methods have only a small effect on μ_s provided that a sufficiently large number of grains is used and that there is some means of preventing grains from rolling away (such as a rim or a rough bed, see figure D2). Based on these simulations, we assign an uncertainty of 5% to all μ_s -measurements, including those from different studies and methods.

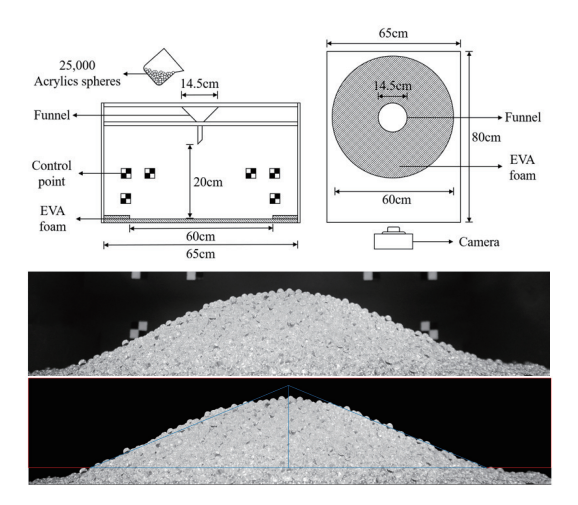


Figure D1. Measurements of μ_s for the data set NC18EXP (Table 1). We slowly poured 25,000 grains onto an elevated disk bounded by a 2*d*-high rim. The angle of repose of the resulting heap is then determined as the base angle of the isosceles triangle that has the same area as the projected heap, averaged over two side-view images separated by a rotation of 90° (Elekesa & Parteli, 2021).

Appendix E Grain-unresolved simulation details

E1 Contact parameters and μ_s in grain-unresolved CFD-DEM simulations

The normal restitution coefficient e_n , tangential contact friction coefficient μ_c , and tangent of the static angle of repose, μ_s (determined as described in figure D2), are $(e_n, \mu_c, \mu_s) = (0.5, 0.4, 0.40)$ for the model of Maurin et al. (2015) and data of Maurin et al. (2018), $(e_n, \mu_c, \mu_s) = (0.5, 0.5, 0.49 - 0.72)$ for the model of Maurin et al. (2015) and data of Monthiller (2019), $(e_n, \mu_c, \mu_s) = (0.9, 0.5, 0.38)$ for the model of Durán et al. (2012), and $(e_n, \mu_c, \mu_s) = (0.3, 0.5, 0.49)$ for the model of Xie et al. (2022).

E2 Drag coefficient

The numerical CFD-DEM models that do not resolve the sub-grain scale rely on semiempirical relations for fluid-particle interactions. They consider buoyancy and drag forces on spheres or composite grains consisting of non-overlapping component spheres, but neglect lift forces. Following Sun et al. (2017), the drag force is modeled as the total force on all component spheres:

$$\boldsymbol{F_D} = \sum_{i} \frac{1}{8} \rho_f \pi d_i^2 \left[\left(\frac{\Re_c \nu}{d_i \epsilon^{p_1}} \right)^{1/m} + \left(\frac{C_D^{\infty} |\boldsymbol{u_r}|}{\epsilon^{p_2}} \right)^{1/m} \right]^m \boldsymbol{u_r}, \tag{E1}$$

where d_i is the diameter of the i-th component sphere, $\boldsymbol{u_r}$ the fluid-particle velocity difference, and \Re_c , C_D^{∞} , m, p_1 , and p_2 are empirical parameters. They are $(\Re_c, C_C^{\infty}, m, p_1, p_2) = (24.4, 0.4, 1, 3.1, 3.1)$ in Maurin et al. (2015), $(\Re_c, C_C^{\infty}, m, p_1, p_2) = (24, 0.5, 2, 0, 0)$ in Durán et al. (2012) (nominal), $(\Re_c, C_C^{\infty}, m, p_1, p_2) = (96, 2, 2, 0, 0)$ in Durán et al. (2012) (enhanced drag), $(\Re_c, C_C^{\infty}, m, p_1, p_2) = (23.04, 0.3969, 2, p, p-1)$ in Xie et al. (2022) (nominal), and $(\Re_c, C_C^{\infty}, m, p_1, p_2) = (69.12, 1.1907, 2, p, p-1)$ in Xie et al. (2022) (enhanced drag), with $p = 3.7 - 0.65 \exp[-(1.5 - \log_{10}(\epsilon |\boldsymbol{u_r}|d_i/\nu))^2/2]$. Dividing equation (E1) by the grain weight $\frac{\pi}{6} \sum_i d_i^3$ leads to an expression for the ratio between the drag acceleration $\boldsymbol{a_D}$ and submerged gravitational acceleration $\tilde{g} \equiv (1-1/s)g$ in terms of nondi-

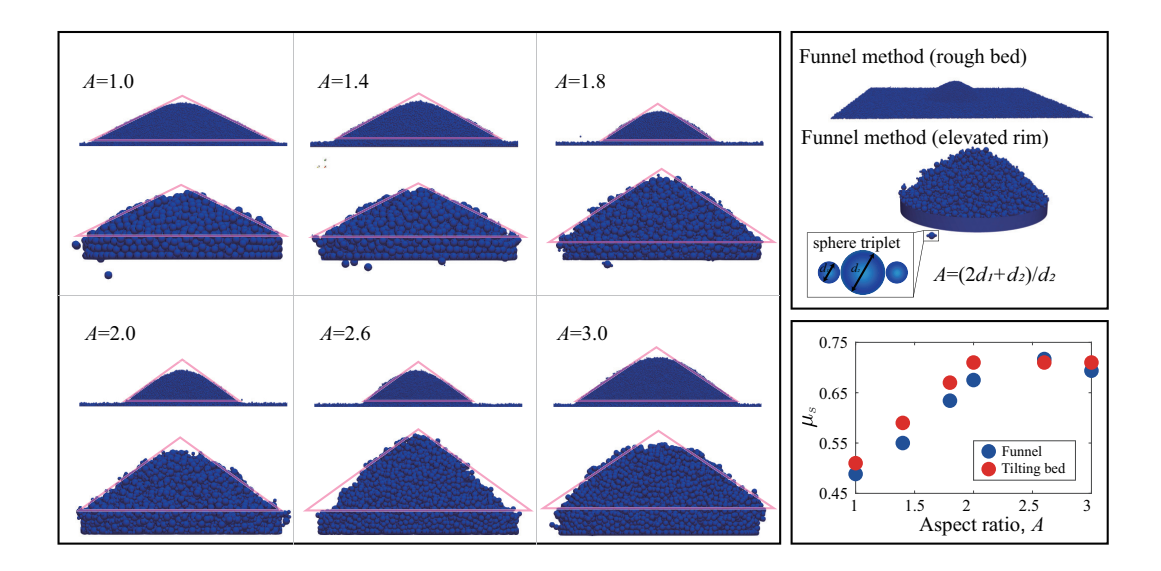


Figure D2. Numerical determination of the static angle of repose. We compare three different methods of measuring the tangent of the static angle of repose, μ_s , for the composite grains (spheres and sphere triplets) used in the grain-unresolved DEM-CFD simulations: slowly pouring a sufficient number of grains onto a rough bed consisting of spheres of the same volumeequivalent sphere diameter d_o (funnel method 1), onto an elevated disk of diameter $24d_o$ bounded by a $2d_o$ -high rim (funnel method 2, exactly as described in Deal et al. (2023)), and tilting the granular bed until the granular bulk moves (tilting method). The most reliable and reproducible results are yielded by funnel method 1, where the angle of repose is determined as the base angle of the isosceles triangle that has the same area as the projected heap, averaged over two sideview images separated by a rotation of 90° (Elekesa & Parteli, 2021). For funnel method 2, the heaps exhibit too irregular shapes when the aspect ratio A becomes too large, making a clear determination of the angle of repose difficult. However, for $A \lesssim 2$, it yields values very close to funnel method 1. The tilting method also yields similar results as funnel method 1, though it is sometimes difficult to distinguish between bulk and isolated-grain motion. We therefore decided to use funnel method 1 as the standard procedure to determine μ_s in the grain-unresolved DEM-CFD simulations.

mensionalized quantities:

$$\frac{\boldsymbol{a_D}}{\tilde{g}} = \frac{3}{4} \left[\left(\frac{\Re_c}{\widetilde{G}a\epsilon^{p_1}} \right)^{1/m} + \left(\frac{C_D^{\infty}|\tilde{\boldsymbol{u_r}}|}{\epsilon^{p_2}} \right)^{1/m} \right]^m \tilde{\boldsymbol{u_r}}, \tag{E2}$$

where $\tilde{\boldsymbol{u}}_r \equiv \boldsymbol{u}_r/\sqrt{s\tilde{g}d}$, with $d \equiv \frac{3}{2}V_p/A_p^{\max} = \sum_i d_i^3/\sum_i d_i^2$, is the nondimensionalized fluid-particle velocity difference and

$$\widetilde{Ga} \equiv \frac{\sqrt{(\sum_{i} d_{i}^{2})(\sum_{i} d_{i}^{3})}}{\sum_{i} d_{i}} \sqrt{s\tilde{g}} / \nu \tag{E3}$$

a quantity similar to the Galileo number. From equation (E2), one obtains the nondimensionalized settling velocity \tilde{v}_s of a single composite grain in quiescent fluid ($\epsilon = 1$) as (Pähtz et al., 2021)

$$\tilde{v}_s = \left[\sqrt{\frac{1}{4} \sqrt[m]{\left(\frac{\Re_c}{C_D^{\infty} \widetilde{Ga}}\right)^2 + \sqrt[m]{\frac{4}{3C_D^{\infty}}} - \frac{1}{2} \sqrt[m]{\frac{\Re_c}{C_D^{\infty} \widetilde{Ga}}} \right]^m}$$
 (E4)

and subsequently the drag coefficient as

$$C_D = \frac{4(s-1)gd}{3v_s^2} = \frac{4}{3\tilde{v}_s^2}.$$
 (E5)

Here we used that a composite grain is treated as if the projected area of all its component spheres is always, regardless of its orientation relative to the flow, fully exposed to the flow, which follows from equation (E1). That is, the total projected area seen by the flow, $A_p = \frac{\pi}{4} \sum_i d_i^2$, is constant, and therefore $A_p^{\text{eff}} = A_p^{\text{max}}$.

Appendix F Sphere-normalized drag coefficient after Deal et al.

Deal et al. (2023) defined the sphere-normalized drag coefficient C^* as

$$C^* \equiv S_f v_o^2 / v_s^2, \tag{F1}$$

where v_o is the theoretical value of the settling velocity of spheres, given by (Dietrich, 1982; Deal et al., 2023)

$$v_{o*} = -3.81564 + 1.94593D_* - 0.09016D_*^2 - 0.00855D_*^3 + 0.00075D_*^4,$$
 (F2)

with $v_{o*} \equiv \log_{10} v_o^3/[(s-1)g\nu]$, $D_* \equiv \log_{10}(s-1)gd_o^3/\nu^2$. Since these expressions are based on the volume-equivalent sphere diameter d_o , as opposed to the shortest grain axis c_g in our model, C^* is linked to the drag coefficient C_D in equation (17) through $C^* = C_D d_o/(C_o c_g)$, where $C_o \equiv 4(s-1)gd_o/(3v_o^2)$.

References

- Ancey, C. (2020). Bedload transport: a walk between randomness and determinism. Part 1. The state of the art. *Journal of Hydraulic Research*, 58(1), 1-17. doi: 10.1080/00221686.2019.1702594
- Ancey, C., & Recking, A. (2023). Scaling behavior of bedload transport: what if bagnold was right? Earth-Science Reviews, 246, 104571. doi: 10.1016/j.earscirev.2023.104571
- Antonia, R., & Pearson, B. (2000). Reynolds number dependence of velocity structure functions in a turbulent pipe flow. Flow, Turbulence and Combustion, 64(2), 95-117. doi: 10.1023/A:1009900120828
- Armanini, A., & Cavedon, V. (2019). Bed-load through emergent vegetation. Advances in Water Resources, 129, 250-259. doi: 10.1016/j.advwatres.2019.05.021
- Auel, C., Albayrak, I., & Boes, R. M. (2014). Turbulence characteristics in supercritical open channel flows: Effects of froude number and aspect ratio. Journal of Hydraulic Engineering, 140(4), 04014004. doi: 10.1061/(ASCE)HY.1943 -7900.0000841
- Bagnold, R. A. (1956). The flow of cohesionless grains in fluid. *Philosophical Transactions of the Royal Society London A*, 249(964), 235-297. doi: 10.1098/rsta.1956.0020
- Baker, V. R., Hamilton, C. W., Burr, D. M., Gulick, V. C., Komatsu, G., Luo, W., ... Rodriguez, J. (2015). Fluvial geomorphology on Earth-like planetary surfaces: A review. *Geomorphology*, 245, 149-182. doi: 10.1016/j.geomorph.2015.05.002
- Beakawi Al-Hashemi, H. M., & Baghabra Al-Amoudi, O. S. (2018). A review on the angle of repose of granular materials. *Powder Technology*, 330, 397-417. doi: 10.1016/j.powtec.2018.02.003
- Benavides, S. J., Deal, E., Venditti, J. G., Bradley, R., Zhang, Q., Kamrin, K., & Perron, J. T. (2023). How fast or how many? Sources of intermittent sediment transport. *Geophysical Research Letters*, 50(9), e2022GL101919. doi: 10.1029/2022GL101919

- Biegert, E., Vowinckel, B., & Meiburg, E. (2017). A collision model for grain-resolving simulations of flows over dense, mobile, polydisperse granular sediment beds. *Journal of Computational Physics*, 340, 105-127. doi: 10.1016/j.jcp.2017.03.035
- Boyer, F., Guazzelli, É., & Pouliquen, O. (2011). Unifying suspension and granular rheology. *Physical Review Letters*, 107(18), 188301. doi: 10.1103/PhysRevLett .107.188301
- Carrillo, V., Petrie, J., Timbe, L., Pacheco, E., Astudillo, W., Padilla, C., & Cisneros, F. (2022). Validation of an experimental procedure to determine bedload transport rates in steep channels with coarse sediment. Water, 13, 672. doi: 10.3390/w13050672
- Charru, F., Andreotti, B., & Claudin, P. (2013). Sand ripples and dunes. *Annual Review of Fluid Mechanics*, 45, 469-493. doi: 10.1146/annurev-fluid-011212 -140806
- Chauchat, J. (2018). A comprehensive two-phase flow model for unidirectional sheetflows. Journal of Hydraulic Research, 56(1), 15-28. doi: 10.1080/00221686.2017. 1289260
- Chen, Y., Durán, O., & Pähtz, T. (2025). On the testing of grain shape corrections to bedload transport equations with grain-resolved numerical simulations. EGUsphere, 2025, 1-14. Retrieved from https://egusphere.copernicus.org/preprints/2025/egusphere-2025-4932/doi: 10.5194/egusphere-2025-4932
- Chepil, W. S. (1958). The use of evenly spaced hemispheres to evaluate aerodynamic forces on a soil surface. *Transcripts of the American Geophysical Union*, 39, 397-403.
- Chepil, W. S. (1961). The use of spheres to measure lift and drag on wind-eroded soil grains. Soil Science Society of America Journal, 25(5), 343-345. doi: 10.2136/sssaj1961.03615995002500050011x
- Clark, A. H., Shattuck, M. D., Ouellette, N. T., & O'Hern, C. S. (2017). Role of grain dynamics in determining the onset of sediment transport. *Physical Review Fluids*, 2(3), 034305. doi: 10.1103/PhysRevFluids.2.034305
- Deal, E., Venditti, J. G., Benavides, S. J., Bradley, R., Zhang, Q., Kamrin, K., & Perron, J. T. (2023). Grain shape effects in bed load sediment transport. Nature, 613, 298-302. doi: 10.1038/s41586-022-05564-6
- Dhont, B., & Ancey, C. (2018). Are bedload transport pulses in gravel bed rivers created by bar migration or sediment waves? Geophysical Research Letters, 45(11), 5501-5508. doi: 10.1029/2018GL077792
- Dietrich, W. E. (1982). Settling velocity of natural particles. Water Resources Research, 18(6), 1615-1626. doi: 10.1029/WR018i006p01615
- Durán, O., Andreotti, B., & Claudin, P. (2012). Numerical simulation of turbulent sediment transport, from bed load to saltation. *Physics of Fluids*, 24 (10), 103306. doi: 10.1063/1.4757662
- Durán Vinent, O., Andreotti, B., Claudin, P., & Winter, C. (2019). A unified model of ripples and dunes in water and planetary environments. *Nature Geoscience*, 12, 345-350. doi: 10.1038/s41561-019-0336-4
- Einstein, H. A. (1942). Formulas for the transportation of bedload. *Transactions of ASCE*, 107, 561-597. doi: 10.1061/TACEAT.0005468
- Elekesa, F., & Parteli, E. J. R. (2021). An expression for the angle of repose of dry cohesive granular materials on earth and in planetary environments. Proceedings of the National Academy of Sciences of the United States of America, 118(38), e2107965118. doi: 10.1073/pnas.2107965118
- Frey, P. (2014). Particle velocity and concentration profiles in bedload experiments on a steep slope. *Earth Surface Processes and Landforms*, 39(5), 646-655. doi: 10.1002/esp.3517
- Frey, P., Dufresne, M., Böhm, T., Jodeau, M., & Ancey, C. (2006). Experimental

- study of bed load on steep slopes. In *River flow 2006* (p. 887-893). London, UK: Taylor & Francis Group.
- Gioia, G., & Bombardelli, F. A. (2002). Scaling and similarity in rough channel flows. *Physical Review Letters*, 88(1), 014501. doi: 10.1103/PhysRevLett.88.014501
- Gioia, G., & Pinaki Chakraborty. (2006). Turbulent friction in rough pipes and the energy spectrum of the phenomenological theory. *Physical Review Letters*, 96(4), 044502. doi: 10.1103/PhysRevLett.96.044502
- Guo, J. (2015). Sidewall and non-uniformity corrections for flume experiments. Journal of Hydraulic Research, 53(2), 218-229. doi: 10.1080/00221686.2014.971449
- Guo, J. (2017). Exact procedure for Einstein-Johnson's sidewall correction in open channel flow. Journal of Hydraulic Engineering, 143(4), 06016027. doi: 10 .1061/(ASCE)HY.1943-7900.0001260
- Jain, R., Tschisgale, S., & Fröhlich, J. (2020). Effect of particle shape on bedload sediment transport in case of small particle loading. *Meccanica*, 55, 299-315. doi: 10.1007/s11012-019-01064-6
- Jain, R., Tschisgale, S., & Fröhlich, J. (2021). Impact of shape: Dns of sediment transport with non-spherical particles. Journal of Fluid Mechanics, 916, A38. doi: 10.1016/j.advwatres.2019.05.021
- Johnson, J. W. (1942). The importance of considering sidewall friction in bed-load investigations. Civil Engineering, 12, 329-332.
- Kidanemariam, A. G. (2016). The formation of patterns in subaqueous sediment (Doctoral dissertation, Karlsruhe Institute of Technology, Karlsruhe, Germany). Retrieved from https://www.ksp.kit.edu/site/books/m/10.5445/KSP/1000054986/
- Kidanemariam, A. G., & Uhlmann, M. (2017). Formation of sediment patterns in channel flow: minimal unstable systems and their temporal evolution. *Journal of Fluid Mechanics*, 818, 716-743. doi: 10.1017/jfm.2017.147
- Li, X., Balachandar, S., Lee, H., & Bai, B. (2019). Fully resolved simulations of a stationary finite-sized particle in wall turbulence over a rough bed. *Physical Review Fluids*, 4(9), 094302. doi: 10.1103/PhysRevFluids.4.094302
- Matoušek, V., & Zrostlík, Š. (2020). Collisional transport model for intense bed load. Journal of Hydrology and Hydromechanics, 68(1), 60-69. doi: 10.2478/johh-2019-0027
- Maurin, R., Chauchat, J., Chareyre, B., & Frey, P. (2015). A minimal coupled fluid-discrete element model for bedload transport. *Physics of Fluids*, 27(11), 113302. doi: 10.1063/1.4935703
- Maurin, R., Chauchat, J., & Frey, P. (2018). Revisiting slope influence in turbulent bedload transport: consequences for vertical flow structure and transport rate scaling. *Journal of Fluid Mechanics*, 839, 135-156. doi: 10.1017/jfm.2017.903
- Monthiller, R. (2019). Particle shape influence on turbulent bedload transport (Unpublished master's thesis). ENSEEIHT, University of Toulouse, Toulouse, France.
- Ni, W. J., & Capart, H. (2018). Stresses and drag in turbulent bed load from refractive index-matched experiments. Geophysical Research Letters, 45, 7000-7009. doi: 10.1029/2018GL077571
- Pähtz, T., Chen, Y., Rui, Z., Tholen, K., & He, Z. (2025). Coarse-graining particulate two-phase flow. https://doi.org/10.48550/arXiv.2308.09661.
- Pähtz, T., & Durán, O. (2018a). The cessation threshold of nonsuspended sediment transport across aeolian and fluvial environments. *Journal of Geophysical Research: Earth Surface*, 123(8), 1638-1666. doi: 10.1029/2017JF004580
- Pähtz, T., & Durán, O. (2018b). Universal friction law at granular solid-gas transition explains scaling of sediment transport load with excess fluid shear stress. Physical Review Fluids, 3(10), 104302. doi: 10.1103/PhysRevFluids.3.104302

- Pähtz, T., & Durán, O. (2020). Unification of aeolian and fluvial sediment transport rate from granular physics. *Physical Review Letters*, 124(16), 168001. doi: 10.1103/PhysRevLett.124.168001
- Pähtz, T., Liu, Y., Xia, Y., Hu, P., He, Z., & Tholen, K. (2021). Unified model of sediment transport threshold and rate across weak and intense subaqueous bedload, windblown sand, and windblown snow. *Journal of Geophysical Research: Earth Surface*, 126(4), e2020JF005859. doi: 10.1029/2020JF005859
- Poggiali, V., Mastrogiuseppe, M., Hayes, A. G., Seu, R., Birch, S. P. D., Lorenz, R., . . . Hofgartner, J. D. (2016). Liquid-filled canyons on titan. *Geophysical Research Letters*, 43(15), 7887-7894. doi: 10.1002/2016GL069679
- Rebai, D., Berzi, D., Ballio, F., & Matousek, V. (2022). Experimental comparison of inclined flows with and without intense sediment transport: Flow resistance and surface elevation. *Journal of Hydraulic Engineering*, 148(12), 04022026. doi: 10.1061/(ASCE)HY.1943-7900.0002024
- Recking, A. (2010). A comparison between flume and field bed load transport data and consequences for surface-based bed load transport prediction. Water Resources Research, 46(3), W03518. doi: 10.1029/2009WR008007
- Rui, Z., Chen, Y., Pähtz, T., Tholen, K., & He, Z. (2025). On buoyancy in disperse two-phase flow and its impact on well-posedness of two-fluid models. https://doi.org/10.48550/arXiv.2507.21602.
- Schieber, J. (2016). Mud re-distribution in epicontinental basins Exploring likely processes. *Marine and Petroleum Geology*, 71, 119-133. doi: 10.1016/j.marpetgeo.2015.12.014
- Shchepetkina, A., Gingras, M. K., Mángano, M. G., & Buatois, L. A. (2019). Fluvio-tidal transition zone: Terminology, sedimentological and ichnological characteristics, and significance. *Earth-Science Reviews*, 192, 214-235. doi: 10.1016/j.earscirev.2019.03.001
- Shi, P., & Rzehak, R. (2019). Lift forces on solid spherical particles in unbounded flows. *Chemical Engineering Science*, 208, 115145. doi: 10.1016/j.ces.2019.08.003
- Song, T. (1994). Velocity and turbulence distribution in nonuniform and unsteady open-channel flow (Unpublished doctoral dissertation). Swiss Federal Institute of Technology EPFL, Lausanne, Switzerland.
- Song, T., & Chiew, Y. M. (2001). Turbulence measurement in non-uniform openchannel flow using acoustic Doppler velocimeter (ADV). *Journal of Engineer*ing Mechanics, 127(3), 219-232. doi: 10.1061/(ASCE)0733-9399(2001)127: 3(219)
- Sun, R., Xiao, H., & Sun, H. (2017). Realistic representation of grain shapes in CFD-DEM simulations of sediment transport with a bonded-sphere approach. Advances in Water Resources, 107, 421-438. doi: 10.1016/j.advwatres.2017.04.015
- Tennekes, H., & Lumley, J. L. (1972). A first course in turbulence. MIT Press, Cambridge, MA.
- Vanoni, V. A., & Brooks, N. H. (1957). Laboratory studies of the roughness and suspended load of alluvial streams (No. E-68). California Institute of Technology, Pasadena, CA. Retrieved from https://authors.library.caltech.edu/records/zgm6h-att56
- Vowinckel, B., Biegert, E., Meiburg, E., Aussillous, P., & Guazzelli, E. (2021). Rheology of mobile sediment beds sheared by viscous, pressure-driven flows. Journal of Fluid Mechanics, 921, A20. doi: 10.1017/jfm.2021.457
- Wiberg, P. L., & Smith, J. D. (1987). Calculations of the critical shear stress for motion of uniform and heterogeneous sediments. Water Resources Research, 23(8), 1471-1480. doi: 10.1029/WR023i008p01471
- Xie, J., Hu, P., Pähtz, T., He, Z., & Cheng, N. (2022). Fluid-particle interaction regimes during the evolution of turbidity currents from a cou-

- pled les/dem model. Advances in Water Resources, 163, 104171. doi: 10.1016/j.advwatres.2022.104171
- Yager, E. M., Venditti, J. G., Smith, H. J., & Schmeeckle, M. W. (2018). The trouble with shear stress. *Geomorphology*, 323, 41-50. doi: 10.1016/j.geomorph.2018.09.008
- Yang, S. Q., Lim, S. Y., & McCorquodale, J. A. (2005). Investigation of near wall velocity in 3-d smooth channel flows. Journal of Hydraulic Research, 43(2), 149-157. doi: 10.1080/00221686.2005.9641231
- Zhang, Q., Deal, E., Perron, J. T., Venditti, J. G., Benavides, S. J., Rushlow, M., & Kamrin, K. (2022). Fluid-driven transport of round sediment particles: From discrete simulations to continuum modeling. *Journal of Geophysical Research: Earth Surface*, 127(7), e2021JF006504. doi: 10.1029/2021JF006504
- Zhang, Q., Deal, E., Perron, J. T., Venditti, J. G., Benavides, S. J., Rushlow, M., & Kamrin, K. (2025). Discrete simulations of fluid-driven transport of naturally shaped sediment particles. *Journal of Geophysical Research: Earth Surface*, 130(5), e2024JF007937. doi: 10.1029/2024JF007937